

# Primordial black holes and gravitational waves induced by exponential-tailed perturbations

Katsuya T. Abe,<sup>a</sup> Ryoto Inui,<sup>a</sup> Yuichiro Tada,<sup>a,b,c</sup> and Shuichiro Yokoyama<sup>d,e</sup>

<sup>a</sup>Department of Physics, Nagoya University,  
Furo-cho Chikusa-ku, Nagoya 464-8602, Japan

<sup>b</sup>Institute for Advanced Research, Nagoya University,  
Furo-cho Chikusa-ku, Nagoya 464-8601, Japan

<sup>c</sup>Theory Center, IPNS, KEK,  
1-1 Oho, Tsukuba, Ibaraki 305-0801, Japan

<sup>d</sup>Kobayashi Maskawa Institute, Nagoya University,  
Furo-cho Chikusa-ku, Nagoya 464-8602, Japan

<sup>e</sup>Kavli IPMU (WPI), UTIAS, The University of Tokyo,  
5-1-5 Kashiwanoha, Kashiwa, Chiba 277-8583, Japan

E-mail: [abe.katsuya.f3@s.mail.nagoya-u.ac.jp](mailto:abe.katsuya.f3@s.mail.nagoya-u.ac.jp), [inui.ryoto.a3@s.mail.nagoya-u.ac.jp](mailto:inui.ryoto.a3@s.mail.nagoya-u.ac.jp),  
[tada.yuichiro.y8@f.mail.nagoya-u.ac.jp](mailto:tada.yuichiro.y8@f.mail.nagoya-u.ac.jp), [shu@kmi.nagoya-u.ac.jp](mailto:shu@kmi.nagoya-u.ac.jp)

**Abstract.** Primordial black holes (PBHs) whose masses are in  $\sim [10^{-15}M_{\odot}, 10^{-11}M_{\odot}]$  have been extensively studied as a candidate of whole dark matter (DM). One of the probes to test such a PBH-DM scenario is scalar-induced stochastic gravitational waves (GWs) accompanied with the enhanced primordial fluctuations to form the PBHs with frequency peaked in the mHz band being targeted by the LISA mission. In order to utilize the stochastic GWs for checking the PBH-DM scenario, it needs to exactly relate the PBH abundance and the amplitude of the GWs spectrum. Recently in Kitajima et al. [1], the impact of the non-Gaussianity of the enhanced primordial curvature perturbations on the PBH abundance has been investigated based on the peak theory, and they found that a specific non-Gaussian feature called the exponential tail significantly increases the PBH abundance compared with the Gaussian case. In this work, we investigate the spectrum of the induced stochastic GWs associated with PBH DM in the exponential-tail case. In order to take into account the non-Gaussianity properly, we employ the diagrammatic approach for the calculation of the spectrum. We find that the amplitude of the stochastic GW spectrum is slightly lower than the one for the Gaussian case, but it can still be detectable with the LISA sensitivity. We also find that the non-Gaussian contribution can appear on the high-frequency side through their complicated momentum configurations. Although this feature emerges under the LISA sensitivity, it might be possible to obtain information about the non-Gaussianity from GW observation with a deeper sensitivity such as the DECIGO mission.

---

## Contents

<b>1</b>	<b>Introduction</b>	<b>1</b>
<b>2</b>	<b>Exponential-tailed curvature perturbations and primordial black holes</b>	<b>2</b>
<b>3</b>	<b>Gravitational waves induced by scalar perturbations</b>	<b>8</b>
3.1	Gravitational waves induced by the second-order scalar perturbations	9
3.2	Diagrammatic approach	11
3.2.1	Second-order contribution	15
3.2.2	Third-order contributions	15
3.2.3	Fourth-order contributions	16
<b>4</b>	<b>Application to the exponential tail case</b>	<b>20</b>
<b>5</b>	<b>Conclusions</b>	<b>21</b>
<b>A</b>	<b>Detailed computations for fourth-order diagrams</b>	<b>22</b>
A.1	1-convolution C term	22
A.2	1-convolution Z term	25
A.3	CZ term	27

---

## 1 Introduction

Recently, the primordial black hole (PBH), which could be formed in the early Universe, has been attracting much attention. While several formation scenarios have been proposed, one of the most extensively discussed is the formation by the gravitational collapse of over-density regions in the radiation-dominated universe after inflation [2, 3]. One of the interesting characteristics is that the PBHs could be formed with a wide mass range, and PBHs heavier than  $\sim 10^{15}$  g can exist in the present universe as dark matter (DM). In fact, various astronomical observations have placed limits on the abundance of PBHs at various masses (see, e.g., Ref. [4]). As a result, we have a small allowed parameter region for the PBH mass called *PBH mass window*; the possibility that PBH can be whole DM exists only in the case that the mass of PBHs is in  $\sim [10^{-15}M_{\odot}, 10^{-11}M_{\odot}]$ .

One of the promising indirect observables to test such a remaining possibility for PBH to be whole DM would be scalar-induced stochastic gravitational waves (GWs). Since large primordial scalar perturbations are necessary for the formation of PBHs, these perturbations would involve the potential to produce the large-amplitude GWs through the non-linear interactions between the scalar and tensor perturbations, which are called scalar-induced GWs. The GW is becoming a powerful probe for cosmology along with the ongoing/future projects of ground- and space-based GW detectors such as LISA [5], Taiji/Tianqin [6, 7], DECIGO [8], AION/MAGIS [9, 10], LIGO/VIRGO/KAGRA [11], ET/CE [12, 13], and pulsar timing arrays (PTAs) (see, e.g., Ref. [14]). Especially, in LISA and DECIGO, the frequency ranges are corresponding to PBH mass window scales (see, e.g., Refs. [15, 16]). In Ref. [16], the authors suggested the detectability of GWs in LISA in the PBH DM model with an assumption of the Gaussian distribution for the primordial scalar perturbations.

However, to utilize GWs as a probe of the PBH DM model, the statistical nature of the primordial perturbations such as non-Gaussianity should be taken into account properly because it highly affects the connection between the PBH abundance and the amplitude of the scalar-induced GWs (see, e.g., Ref. [17]).

In the standard slow-roll inflationary scenario, the primordial curvature perturbations  $\zeta$  follow the almost Gaussian distribution. On the other hand, recently, the curvature perturbations having the heavier tail in their distribution function than that of the Gaussian have come to be discussed, as the PBHs have become more actively discussed (see, e.g., Ref. [18] and references therein). As a typical example, the primordial curvature perturbations generated in the ultra slow-roll phase during inflation could have amplitudes large enough for PBH formations and also are expected to have *exponential tail* distribution as  $\mathbb{P}(\zeta) \propto e^{-3\zeta}$  in the large  $\zeta$  limit [19–22]. In Ref. [1], the impact of such an exponential tail distribution on the PBH abundance has been carefully studied based on the peak theory, and it is found that the exponential tail significantly enhances the PBH abundance compared with the Gaussian case. When the PBHs accounts for all of DM, this fact leads to a reduction in the required amplitude of the primordial fluctuations, and then it is expected that the induced stochastic GWs associated with the PBHs should be smaller than those in the Gaussian case. Therefore, it needs to investigate whether the induced GWs in the exponential tail case can be still detected or not in the foreseeable observations.

In this work, we evaluate the stochastic GWs induced by the primordial curvature perturbations with the exponential-tail-type non-Gaussianity. In addition to employing the result from Ref. [1], we carefully investigate the possible spectral shape of the induced stochastic GWs by taking the non-Gaussianity of the curvature perturbations into account. To do so, we use the diagrammatic approach that can incorporate such a non-Gaussianity in a perturbative and systematic manner. There are several works that discuss the stochastic GWs induced by the primordial curvature perturbations with the perturbative non-Gaussianities characterized by the so-called non-linearity parameters,  $f_{\text{NL}}$  and  $g_{\text{NL}}$  [23–28] (and Ref. [29] as a recent review). By making use of this diagrammatic approach, we show that all contributions generally can be summarized into nine topologically-independent diagrams and there are still new contributions at the fourth-order of the amplitude of the primordial power as those examined in previous studies.

This paper is organized as follows. In Sec. 2, we will briefly review the generation of the exponential-tailed curvature perturbations and their effect on the abundance of PBHs studied in Ref. [1]. In Sec. 3, we provide a systematic perturbative approach for the calculation of the stochastic GWs induced by the non-Gaussian curvature perturbations, by making use of the diagrams. Then, in Sec. 4, based on the approach given in Sec. 3, we investigate the spectrum of the induced GWs in the exponential tail case and discuss the observability in LISA. Section 5 is devoted to the conclusion. We adopt the natural unit,  $c = \hbar = 1$ , throughout this work.

## 2 Exponential-tailed curvature perturbations and primordial black holes

In the standard scenario of inflation, primordial perturbations originate from the quantum vacuum fluctuation of the inflaton fields. It is therefore expected to well follow the Gaussian distribution at the leading order, which is in fact confirmed with high accuracy in the observation of the cosmic microwave background (CMB) [30]. While this is natural because the CMB scale perturbation is well in the perturbative range as its amplitude is the order

of  $10^{-5}$ , it is however non-trivial whether the Gaussian assumption is valid for PBHs, the object related to the order-unity perturbation. In this section, we review the significant non-Gaussian feature called *the exponential tail* and its effect on the PBH abundance.

In order to deal with the nonlinear feature of gravity on the primordial metric perturbation, the so-called  $\delta N$  formalism is useful [31–34]. Under the assumptions of the separate universe and the energy conservation, the superHubble inflaton perturbation  $\delta\phi$  can be non-perturbatively converted to the conserved curvature perturbation  $\zeta$  on the uniform density slice as the difference  $\delta N$  in the e-foldings  $N$  from the initial flat slice (no perturbation in the spatial curvature) to the final uniform density slice [35]. One then imagines that an extremely large  $\zeta$  or  $\delta N$  can be realized in a so-called reproductive region. In the eternal inflation for example [36–41], the low probability of the large  $N$  is compensated by the volume factor  $a^3 \propto e^{3N}$  [42], which means that such a probability decays only exponentially  $\propto e^{-3N}$  rather than the Gaussian in that case. Such a slow decay of the large- $\zeta$  probability may happen in a wider class of inflation. If the decay of the large- $\zeta$  probability is slower than the Gaussian, the estimation of the PBH abundance can be significantly altered from the one under the Gaussian assumption.

Though the precise probability should be calculated taking all quantum noise into account in, e.g., the stochastic approach (see, e.g., Refs. [31, 43–51] for the first papers on this approach, and also Refs. [52–59] for its application to the exponential tail), qualitative features are often extracted by a simple assumption that only one noise gives a dominant contribution and the other dynamics is well approximated by the one without noise [19, 60–62]. Let us also focus on the extremely-flat-potential region, i.e., the ultra slow-roll phase to make perturbations large. There, the equation of motion (EoM) for the background homogeneous mode of inflaton  $\phi_0$  is approximated as

$$\frac{d^2\phi_0}{dN^2} + 3\frac{d\phi_0}{dN} \simeq 0, \quad H \simeq \text{const.}, \quad (2.1)$$

where  $H$  is the Hubble parameter, and we used e-foldings  $N(t) = \int_{t_i}^t H dt$  from some initial time  $t_i$  to  $t$  as the time variable. It can be easily solved as

$$\phi_0(N) = \phi_i + \frac{\pi_i}{3}(1 - e^{-3N}), \quad \Leftrightarrow \quad N(\phi_0 | \phi_i) = -\frac{1}{3} \ln \left( 1 - 3\frac{\phi_0 - \phi_i}{\pi_i} \right), \quad (2.2)$$

with the initial field value  $\phi_i = \phi_0|_{t_i}$  and momentum  $\pi_i = d\phi_0/dN|_{t_i}$ .  $N(\phi_0 | \phi_i)$  denotes the e-foldings from  $\phi_i$  to  $\phi_0$ . Let us then assume that inflation ends or it is rapidly followed by the ordinary slow-roll phase at the end point  $\phi_f$  and the total curvature perturbation is mainly given by the time difference between  $\phi_i$  and  $\phi_f$  due to the shift  $\delta\phi_i$  at  $\phi_i$  keeping the momentum intact. That is, the curvature perturbation is simply given by

$$\zeta = \delta N = N(\phi_f | \phi_i + \delta\phi_i) - N(\phi_f | \phi_i) = -\frac{1}{3} \ln \left( 1 + 3\frac{\delta\phi_i}{\pi_f} \right), \quad (2.3)$$

where  $\pi_f = \pi_i e^{-3N(\phi_f|\phi_i)} = \pi_i - 3(\phi_f - \phi_i)$  is the momentum at  $\phi_f$  without noise. Supposing the inflaton's noise  $\delta\phi_i$  follows the Gaussian distribution and defining the Gaussian part of the curvature perturbation by  $\zeta_g = -\delta\phi_i/\pi_f$ , the full curvature perturbation is understood as a nonlinear transformation of the Gaussian field in this case [19–22]:

$$\zeta(\mathbf{x}) = -\frac{1}{3} \ln(1 - 3\zeta_g(\mathbf{x})). \quad (2.4)$$

In the small perturbation region  $|\zeta| \ll 1$ , the full curvature perturbation is well approximated by the Gaussian part  $\zeta_g$  with perturbative corrections as can be seen in its series expansion,

$$\zeta = -\frac{1}{3} \ln(1 - 3\zeta_g) = \zeta_g + \frac{3}{2}\zeta_g^2 + 3\zeta_g^3 + \frac{27}{4}\zeta_g^4 + \frac{81}{5}\zeta_g^5 + \mathcal{O}(\zeta_g^6). \quad (2.5)$$

However, it is obviously non-Gaussian essentially for a large enough value  $|\zeta| \gtrsim 1$ . In fact, the probability density function of  $\zeta$  can be inferred from that of  $\zeta_g$  with the chain rule as

$$\mathbb{P}_\zeta(\zeta) = \left| \frac{d\zeta_g}{d\zeta} \right| \mathbb{P}_{\zeta_g}(\zeta_g) = e^{-3\zeta} \mathbb{P}_{\zeta_g}(\zeta_g), \quad (2.6)$$

making use of the inverse relation  $\zeta_g = (1 - e^{-3\zeta})/3$  of Eq. (2.4). In the large value limit  $\zeta \rightarrow +\infty$  or equivalently  $\zeta_g \rightarrow 1/3$ , the probability only decays exponentially as  $\mathbb{P}_\zeta(\zeta) \propto e^{-3\zeta}$  contrary to the Gaussian  $\propto e^{-\zeta^2/2\langle\zeta^2\rangle}$ .<sup>1</sup> This is a simple example of the exponential-tailed curvature perturbation. The decay rate  $\Lambda := -d \ln \mathbb{P}_\zeta / d\zeta$  ( $= 3$  in this case) can depend on the details of the model, such as the potential smoothness around  $\phi_f$  for example (see Refs. [19–21]). Heavier tails such that  $\lim_{\zeta \rightarrow +\infty} \Lambda = 0$  have been also proposed [60–62].

If the large- $\zeta$  probability is much amplified than the Gaussian one due to the exponential/heavy tail, the PBH abundance can be significantly altered from the prediction under the Gaussian assumption. The proper abundance taking account of the exponential tail can be calculated in, e.g., the so-called peak theory [63] (see Refs. [1, 64–67] for its application to the PBH mass function). While we refer readers to Ref. [1] for details, let us briefly review the approach.

Once the functional form of  $\zeta$  is fixed as Eq. (2.4), all phenomena caused by the perturbations are statistically deterministic in principle. In particular, it is understood that the profile around a very high peak of the Gaussian field  $\zeta_g$  is typically spherical-symmetric and given by

$$\hat{\zeta}_g = \tilde{\mu}_2 \left[ \frac{1}{1 - \gamma_3^2} \left( \psi_1(r) + \frac{1}{3} R_3^2 \Delta \psi_1(r) \right) - \frac{\tilde{k}_3^2}{\gamma_3(1 - \gamma_3^2)} \left( \gamma_3^2 \psi_1(r) + \frac{1}{3} R_3^2 \Delta \psi_1(r) \right) \right] + \zeta_g^\infty, \quad (2.7)$$

with three dimensionless combined-Gaussian variables  $\tilde{\mu}_2$ ,  $\tilde{k}_3$ , and  $\zeta_g^\infty$ , and characteristics

$$\sigma_n^2 = \int \frac{dk}{k} k^{2n} \mathcal{P}_g(k), \quad \psi_n(r) = \frac{1}{\sigma_n^2} \int \frac{dk}{k} k^{2n} \frac{\sin(kr)}{kr} \mathcal{P}_g(k), \quad \gamma_3 = \frac{\sigma_3^2}{\sigma_2 \sigma_4}, \quad R_3 = \frac{\sqrt{3} \sigma_3}{\sigma_4}, \quad (2.8)$$

determined by  $\zeta_g$ 's power spectrum

$$\mathcal{P}_g(k) = \frac{k^3}{2\pi^2} \int d^3x e^{-i\mathbf{k}\cdot\mathbf{x}} \left\langle \zeta_g\left(\frac{\mathbf{x}}{2}\right) \zeta_g\left(-\frac{\mathbf{x}}{2}\right) \right\rangle. \quad (2.9)$$

---

<sup>1</sup>Note that the probability  $\mathbb{P}_\zeta$  is not normalized to unity,  $\int \mathbb{P}_\zeta d\zeta < 1$ , as  $\zeta = -\frac{1}{3} \ln(1 - 3\zeta_g)$  is defined only for  $\zeta_g \in (-\infty, 1/3)$ .  $\zeta_g \geq 1/3$  corresponds to an eternally inflating baby universe in the current setup and can be also seen as a PBH from the outer universe [21]. The proper renormalization might be done by taking account of the cumulative noise in the stochastic formalism. We simply neglect such a contribution in this work as it is probabilistically suppressed.

Roughly speaking, three variables  $\tilde{\mu}_2$ ,  $\tilde{k}_3$ , and  $\zeta_g^\infty$  indicate the peak height, width, and overall offset, respectively. The (comoving) number density of such a peak is statistically given by

$$n_{\text{pk}} d\tilde{\mu}_2 d\tilde{k}_3 d\zeta_g^\infty = \frac{2 \cdot 3^{3/2} \sigma_2^2 \sigma_4^3}{(2\pi)^{3/2} \sigma_1^4 \sigma_3^3} \tilde{\mu}_2 \tilde{k}_3 f\left(\frac{\sigma_2}{\sigma_1} \tilde{\mu}_2 \tilde{k}_3^2\right) \mathbb{P}_1^{(3)}\left(\frac{\sigma_2}{\sigma_1} \tilde{\mu}_2, \frac{\sigma_2}{\sigma_1} \tilde{\mu}_2 \tilde{k}_3^2\right) \mathbb{P}_\infty(\zeta_g^\infty) d\tilde{\mu}_2 d\tilde{k}_3 d\zeta_g^\infty, \quad (2.10)$$

where

$$\begin{aligned} f(\xi) &= \frac{1}{2} \xi (\xi^2 - 3) \left( \operatorname{erf} \left[ \frac{1}{2} \sqrt{\frac{5}{2}} \xi \right] + \operatorname{erf} \left[ \sqrt{\frac{5}{2}} \xi \right] \right) \\ &\quad + \sqrt{\frac{2}{5\pi}} \left\{ \left( \frac{8}{5} + \frac{31}{4} \xi^2 \right) \exp \left[ -\frac{5}{8} \xi^2 \right] + \left( -\frac{8}{5} + \frac{1}{2} \xi^2 \right) \exp \left[ -\frac{5}{2} \xi^2 \right] \right\}, \\ \mathbb{P}_1^{(3)}(\nu, \xi) &= \frac{1}{2\pi \sqrt{1 - \gamma_3^2}} \exp \left[ -\frac{1}{2} \left( \nu^2 + \frac{(\xi - \gamma\nu)^2}{1 - \gamma_3^2} \right) \right], \\ \mathbb{P}_\infty(\zeta_g^\infty) &= \left( \frac{1 - \gamma_3^2}{2\pi D \sigma_0^2} \right)^{1/2} \exp \left[ -\frac{1 - \gamma_3^2}{2D \sigma_0^2} \zeta_g^{\infty 2} \right], \end{aligned} \quad (2.11)$$

with

$$D = 1 - \gamma_1^2 - \gamma_2^2 - \gamma_3^2 + 2\gamma_1\gamma_2\gamma_3, \quad \gamma_1 = \frac{\sigma_1^2}{\sigma_0\sigma_2}, \quad \gamma_2 = \frac{\sigma_2^2}{\sigma_0\sigma_4}. \quad (2.12)$$

The peak profile of the full  $\zeta$  is of course given by

$$\hat{\zeta}(r) = -\frac{1}{3} \ln \left( 1 - 3\hat{\zeta}_g(r) \right), \quad (2.13)$$

with the same number density.

Whether such a peak collapses into a black hole or not can be judged by the mean compaction function, backed by several numerical works [21, 68]. The compaction function is defined by

$$\mathcal{C}(r) = \frac{2}{3} \left[ 1 - (1 + r\hat{\zeta}'(r))^2 \right], \quad (2.14)$$

and the (maximal) mean compaction is given by

$$\bar{\mathcal{C}}_m = \left( 4\pi \int_0^{R(r_m)} \mathcal{C}(r) R^2(r) dR(r) \right) / \left( \frac{4\pi}{3} R^3(r_m) \right), \quad (2.15)$$

with the areal radius  $R(r) = ae^{\zeta(r)}r$  and the radius  $r_m$  corresponding to the (innermost) maximum of  $\mathcal{C}(r)$ . If the mean compaction  $\bar{\mathcal{C}}_m$  exceeds the threshold value  $\bar{\mathcal{C}}_{\text{th}} = 2/5$ , the corresponding peak is supposed to form a PBH.

The mass of the resultant PBH is assumed to follow the scaling relation:

$$M_{\text{PBH}}(\tilde{\mu}_2, \tilde{k}_3, \zeta_g^\infty) = K \left( \tilde{\mu}_2 - \tilde{\mu}_{2,\text{th}}(\tilde{k}_3, \zeta_g^\infty) \right)^p M_H(\tilde{\mu}_2, \tilde{k}_3, \zeta_g^\infty), \quad (2.16)$$

with the universal power  $p \simeq 0.36$  [69–75].  $K$  is the slightly-profile-dependent order-unity coefficient and we uniformly approximate it as  $K \simeq 1$  for simplicity in this paper.  $\tilde{\mu}_{2,\text{th}}(\tilde{k}_3, \zeta_g^\infty)$

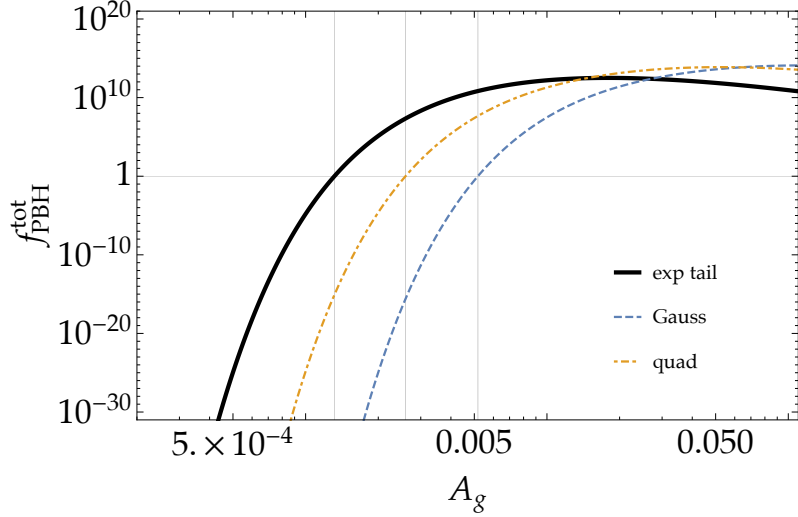


**Figure 1:** the total PBH abundance  $f_{\text{PBH}}^{\text{tot}}$  (2.19) as a function of the perturbation amplitude  $A_g$  in the monochromatic power spectrum case (2.20) for  $k_* = 1.56 \times 10^{12} \text{ Mpc}^{-1}$ . The black thick line is the result of the exponential-tailed perturbation, while the blue dashed and orange dot-dashed correspond to the Gaussian  $\zeta \simeq \zeta_g$  and the quadratic approximation  $\zeta \simeq \zeta_g + (3/2)\zeta_g^2$ , respectively. The vertical thin lines indicate the required amplitude  $A_g = 1.32 \times 10^{-3}$ ,  $2.59 \times 10^{-3}$ , and  $5.17 \times 10^{-3}$  for  $f_{\text{PBH}}^{\text{tot}} = 1$  in each case. The exponential tail feature amplifies the PBH abundance and thus reduces the required perturbation amplitude for given  $f_{\text{PBH}}^{\text{tot}}$ .

is the  $\tilde{\mu}_2$  value on the threshold, i.e.  $\bar{C}_m(\tilde{\mu}_{2,\text{th}}, \tilde{k}_3, \zeta_g^\infty) = \bar{C}_{\text{th}}$ , which depends on the other variables  $\tilde{k}_3$  and  $\zeta_g^\infty$ .  $M_H$  is the Hubble mass at the Hubble reentry of the maximal radius,  $R(r_m)H = 1$ .

With use of this expression of the mass, the PBH number density  $n_{\text{PBH}}(M) d \ln M$  within the mass range of  $[M, Me^{d \ln M}]$  is computed as

$$n_{\text{PBH}}(M) = \int_{\bar{C}_m(\tilde{\mu}_2, \tilde{k}_3, \zeta_g^\infty) > \bar{C}_{\text{th}}} n_{\text{pk}}(\tilde{\mu}_2, \tilde{k}_3, \zeta_g^\infty) \delta(\ln M_{\text{PBH}}(\tilde{\mu}_2, \tilde{k}_3, \zeta_g^\infty) - \ln M) d\tilde{\mu}_2 d\tilde{k}_3 d\zeta_g^\infty. \quad (2.17)$$

The current density ratio  $f_{\text{PBH}}(M)$  of PBHs to total dark matters in this mass bin then reads

$$f_{\text{PBH}}(M) d \ln M = \frac{M n_{\text{PBH}}(M)}{3M_{\text{Pl}}^2 H_0^2 \Omega_{\text{DM}}} d \ln M, \quad (2.18)$$

with the current Hubble parameter  $H_0$  and the dark matter density parameter  $\Omega_{\text{DM}}$ .  $M_{\text{Pl}} = 1/\sqrt{8\pi G}$  is the reduced Planck mass. The total PBH abundance is given by

$$f_{\text{PBH}}^{\text{tot}} = \int f_{\text{PBH}}(M) d \ln M. \quad (2.19)$$

If one simply assumes the monochromatic power spectrum for  $\zeta_g$ ,

$$\mathcal{P}_g(k) = A_g \delta(\ln k - \ln k_*), \quad (2.20)$$

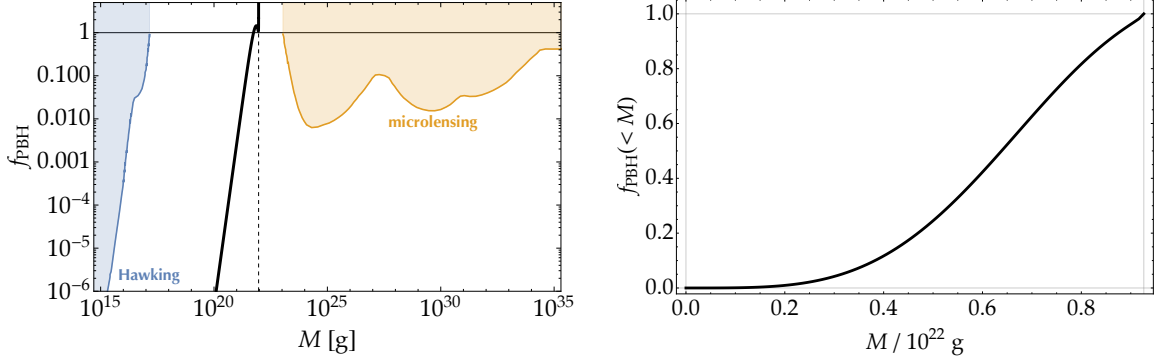


**Figure 2:** *Left:* the corresponding PBH mass function (black) for  $f_{\text{PBH}}^{\text{tot}} = 1$  in the exponential tail case with the observational constraints due to the Hawking radiation (blue) and the gravitational microlensing (orange), taken from Ref. [77] (see also references therein). The mass function is diverging at the maximal mass  $M_{\text{max}} (\simeq 0.926 \times 10^{22} \text{ g}$  in this setup; the vertical black dashed line) due to a characteristic feature of the exponential tail but its integral is converging healthily (see the text). *Right:* the cumulative mass spectrum (2.23) for intuitive understanding of the PBH mass distribution. Gridlines denote  $M = 0$ ,  $M = M_{\text{max}}$ ,  $f_{\text{PBH}}(< M) = 0$ , and  $f_{\text{PBH}}(< M) = 1$ , respectively. One finds  $f_{\text{PBH}}^{\text{tot}} = f_{\text{PBH}}(< M_{\text{max}}) = 1$  indeed.

one finds that the variables  $\tilde{k}_3$  and  $\zeta_g^\infty$  are fixed to 1 and 0 respectively as

$$\mathbb{P}_1^{(3)}\left(\frac{\sigma_2}{\sigma_1^2}\tilde{\mu}_2, \frac{\sigma_2}{\sigma_1^2}\tilde{\mu}_2\tilde{k}_3^2\right) \rightarrow \frac{A_g}{2\tilde{\mu}_2} \frac{1}{\sqrt{2\pi A_g}} e^{-\tilde{\mu}_2^2/(2A_g)} \delta(\tilde{k}_3 - 1), \quad \mathbb{P}_\infty(\zeta_g^\infty) \rightarrow \delta(\zeta_g^\infty). \quad (2.21)$$

Then only  $\tilde{\mu}_2$  remains and the analysis is much simplified. In this case, the PBH mass is sharply distributed around the mass scale corresponding to  $k_*$  (see, e.g., Ref. [76]):

$$M_k(k_*) = 10^{22} \left(\frac{g_*}{106.75}\right)^{-1/6} \left(\frac{k_*}{1.56 \times 10^{12} \text{ Mpc}^{-1}}\right)^{-2} \text{ g}, \quad (2.22)$$

where  $g_*$  is the effective degrees of freedom for energy at the horizon reentry of the mode  $k_*$ . An example result is shown in Fig. 1 for  $k_* = 1.56 \times 10^{12} \text{ Mpc}^{-1}$  (or  $M_k(k_*) = 10^{22} \text{ g}$ ), where we show the total PBH abundance  $f_{\text{PBH}}^{\text{tot}}$  as a function of the perturbation amplitude  $A_g$ . While  $A_g = 5.17 \times 10^{-3}$  is required for  $f_{\text{PBH}}^{\text{tot}} = 1$  if the curvature perturbation is Gaussian, the required amplitude is reduced to  $A_g = 1.32 \times 10^{-3}$  for the exponential-tailed perturbation as expected. The quadratic approximation  $\zeta \simeq \zeta_g + (3/2)\zeta_g^2$  (orange dot-dashed) is better than the simple Gaussian assumption but one sees it is far from enough. Note that, the ratio of the  $A_g$  value between the Gaussian and the exponential tail,  $\left(\frac{1.32 \times 10^{-3}}{5.17 \times 10^{-3}}\right) \sim 0.25$ , would universally hold when  $f_{\text{PBH}} \lesssim 1$ . Since the density parameter of the induced GWs is, at the leading order, proportional to  $A_g^2$ ,  $\Omega_{\text{GW}} \propto A_g^2$ , as we will see below, this universal reduction of  $A_g$  gives the universal relation that the induced GW amplitude in the exponential tail case is  $\sim 6\%$  of the one in the Gaussian tail.

We show the corresponding PBH mass spectrum in the left panel of Fig. 2 with several observational constraints. Interestingly, the mass function has a hard cut and is divergent at  $M_{\text{max}} \simeq 0.926 \times 10^{22} \text{ g}$  shown by the black dashed line as discussed in Ref. [1]. This is because the PBH mass (2.16) is not monotonic in the perturbation amplitude  $\tilde{\mu}_2$  but has a maximum



value  $M_{\max} = M(\tilde{\mu}_{2,\max})$  and hence the Jacobian  $|\mathrm{d} \ln M / \mathrm{d} \tilde{\mu}_2|^{-1}$  from the distribution of  $\tilde{\mu}_2$  to that of  $\ln M$  is divergent at that mass (see the bottom panel of Fig. 6 of Ref. [1]). Noting that the PBH mass behaves quadratically around that point as  $M_{\max} - M \propto (\tilde{\mu}_2 - \tilde{\mu}_{2,\max})^2$ , one finds that the divergence is as slow as  $f_{\mathrm{PBH}} \propto (M_{\max} - M)^{-1/2}$  and hence its integral is healthily convergent. In the right panel of Fig. 2, we plot the cumulative spectrum

$$f_{\mathrm{PBH}}(< M) := \int^M f_{\mathrm{PBH}}(M') \frac{\mathrm{d}M'}{M'}, \quad (2.23)$$

to show the PBH mass distribution more intuitively.

### 3 Gravitational waves induced by scalar perturbations

Let us move on to GWs induced by scalar perturbations  $\zeta$ . We first note that the series expansion of  $\zeta$  given by Eq. (2.5) is expected to work well for the calculation of GWs contrary to the PBH abundance. This is because the amplitude of GWs is mainly determined by the  $\zeta$ 's typical behavior with high probability, i.e.,  $\zeta \sim 0$ , while PBHs is associated with the rare high peaks  $\zeta \gtrsim 1$ . Therefore, we develop the GW calculation method with use of this series expansion in this section. We will see in the next section that the result indeed converges well practically even in the exponential tail case.

We begin with the conformal Newtonian gauge (see Refs. [78–89] for the gauge choice issue). With the assumption that the vector perturbations and the anisotropic stress are negligible, the perturbed metric is defined by

$$\mathrm{d}s^2 = -a(\tau)^2(1 + 2\Phi) \mathrm{d}\tau + a(\tau)^2 \left( (1 - 2\Phi)\delta_{ij} + \frac{1}{2}h_{ij} \right) \mathrm{d}x^i \mathrm{d}x^j, \quad (3.1)$$

where  $\tau$  is the conformal time,  $\Phi$  is the scalar gravitational potential, and  $h_{ij}$  is the transverse traceless tensor perturbation.

We below consider the tensor perturbation  $h$  generated by the second-order effect of the scalar perturbation  $\Phi$ .<sup>2</sup>

We expand the tensor perturbation with the Fourier modes as

$$h_{ij}(\tau, \mathbf{x}) = \sum_{\lambda=+,\times} \int \frac{\mathrm{d}^3k}{(2\pi)^3} e^{i\mathbf{k}\cdot\mathbf{x}} e_{ij}^\lambda(k) h_\lambda(\tau, \mathbf{k}), \quad (3.2)$$

where the two time-independent transverse traceless polarization tensors are defined by

$$\begin{aligned} e_{ij}^+(\mathbf{k}) &= \frac{1}{\sqrt{2}}(e_i(\mathbf{k})e_j(\mathbf{k}) - \bar{e}_i(\mathbf{k})\bar{e}_j(\mathbf{k})), \\ e_{ij}^\times(\mathbf{k}) &= \frac{1}{\sqrt{2}}(e_i(\mathbf{k})\bar{e}_j(\mathbf{k}) + \bar{e}_i(\mathbf{k})e_j(\mathbf{k})), \end{aligned} \quad (3.3)$$

with the two normalized vectors  $e_i(\mathbf{k})$  and  $\bar{e}_i(\mathbf{k})$  orthogonal to each other and to the wave vector  $\mathbf{k}$ .

The tensor power spectrum  $P_{\lambda\lambda'}(\tau, k)$  is defined as

$$\langle h_\lambda(\tau, \mathbf{k}) h_{\lambda'}(\tau, \mathbf{k}') \rangle = (2\pi)^3 \delta^3(\mathbf{k} + \mathbf{k}') P_{\lambda\lambda'}(\tau, k), \quad (3.4)$$

<sup>2</sup> The higher order contributions such as  $h \sim \Phi^3$  and  $\Phi^4$  have been recently discussed in Refs. [90–92]. We will touch on them again later in Sec. 4.

and the dimensionless power spectrum  $\mathcal{P}_{\lambda\lambda'}(\tau, k)$  is given by

$$\mathcal{P}_{\lambda\lambda'}(\tau, k) = \frac{k^3}{2\pi^2} P_{\lambda\lambda'}(\tau, k). \quad (3.5)$$

The energy density of the scalar-induced GWs on the subhorizon scales is evaluated as

$$\rho_{\text{GW}}(\tau) = \int d \ln k \rho_{\text{GW}}(\tau, k) = \frac{M_{\text{Pl}}}{16a^2(\tau)} \overline{\langle h_{ij,k} h_{ij,k} \rangle}, \quad (3.6)$$

where  $h_{ij,k} = \partial_{x^k} h_{ij}$  and the overline stands for the oscillation average. The GW density parameter per logarithmic wavenumber reads

$$\Omega_{\text{GW}}(\tau, k) = \frac{\rho_{\text{GW}}(\tau, k)}{\rho_{\text{tot}}(\tau)} = \sum_{\lambda, \lambda' = +, \times} \Omega_{\text{GW}, \lambda\lambda'} = \frac{1}{48} \left( \frac{k}{a(\tau)H(\tau)} \right)^2 \sum_{\lambda, \lambda' = +, \times} \overline{\mathcal{P}_{\lambda\lambda'}(\tau, k)}. \quad (3.7)$$

Note that the contribution of  $\lambda \neq \lambda'$  will vanish in the parity-conserving universe as we will check either analytically or numerically (see also Appendix A). Since the energy density dilution of GWs is the same as the one of the radiation, i.e.  $\rho \propto a^{-4}$ , unless energy injection by decay or annihilation of particles, the GW density parameter converges to a constant in the deep subhorizon limit during the radiation-dominated (RD) era. We will below calculate this limit value  $\Omega_{\text{GW}}^{\text{RD}}(k) := \Omega_{\text{GW}}(\tau \rightarrow \infty, k)$ . The current density parameter  $\Omega_{\text{GW},0}(k)$  can be simply estimated by multiplying it by the current radiation parameter  $\Omega_{\text{r},0} h^2 \simeq 4.2 \times 10^{-5}$  as  $\Omega_{\text{GW},0}(k) h^2 \simeq \Omega_{\text{GW}}^{\text{RD}}(k) \Omega_{\text{r},0} h^2$ .

### 3.1 Gravitational waves induced by the second-order scalar perturbations

We here review the formulation of GWs induced by the second-order scalar perturbations (see, e.g., Refs. [93, 94] for the details). Note that we only focus on the induced GWs and neglect the primordial tensor perturbations caused by the vacuum fluctuations in this work. In Fourier space, the EoM for GWs including the quadratic terms of  $\Phi$  is given by

$$\partial_\tau^2 h_\lambda(\tau, \mathbf{k}) + 2\mathcal{H}\partial_\tau h_\lambda(\tau, \mathbf{k}) + k^2 h_\lambda(\tau, \mathbf{k}) = 4S_\lambda(\tau, \mathbf{k}), \quad (3.8)$$

where  $S_\lambda(\tau, \mathbf{k})$  is the source term,  $\mathcal{H} = a(\tau)H(\tau)$  is the conformal Hubble parameter. If one adopts the linear relation between the gravitational potential  $\Phi$  and the primordial curvature perturbation  $\zeta$  with the transfer function  $\Phi(k\tau)$  as

$$\Phi(\tau, \mathbf{k}) = \frac{2}{3}\Phi(k\tau)\zeta(\mathbf{k}) \quad \text{in the RD era}, \quad (3.9)$$

the source term  $S_\lambda(\tau, \mathbf{k})$  can be written in terms of  $\zeta$  as

$$S_\lambda(\tau, \mathbf{k}) = \int \frac{d^3q}{(2\pi)^3} Q_\lambda(\mathbf{k}, \mathbf{q}) f(|\mathbf{k} - \mathbf{q}|, q, \tau) \zeta(\mathbf{q}) \zeta(\mathbf{k} - \mathbf{q}). \quad (3.10)$$

Here, the projection factor  $Q_\lambda(\mathbf{k}, \mathbf{q})$  is given by

$$Q_\lambda(\mathbf{k}, \mathbf{q}) = e_{ij}^\lambda(\mathbf{k}) q^i q^j = \frac{q^2}{\sqrt{2}} \sin^2 \theta \times \begin{cases} \cos(2\phi) & (\lambda = +) \\ \sin(2\phi) & (\lambda = \times) \end{cases}, \quad (3.11)$$

for the spherical coordinate expression  $\mathbf{q} = q(\sin \theta \cos \phi, \sin \theta \sin \phi, \cos \theta)^T$  with  $\mathbf{k}$  in the  $z$ -direction, and the source factor  $f(p, q, \tau)$  is

$$f(p, q, \tau) = \frac{4}{9} \left[ 3\Phi(p\tau)\Phi(q\tau) + \Phi'(p\tau)\Phi'(q\tau) + (\Phi(p\tau)\Phi'(q\tau) + \Phi'(p\tau)\Phi(q\tau)) \right], \quad (3.12)$$

in the RD era where  $\Phi'(x) = d\Phi(x)/d \ln x$ . The transfer function in the RD era is given by<sup>3</sup>

$$\Phi(x) = -\frac{9}{x^2} \left( \frac{\sin(x/\sqrt{3})}{x/\sqrt{3}} - \cos(x/\sqrt{3}) \right). \quad (3.13)$$

Adopting the Green's function method to solve Eq. (3.8), the particular solution of the induced GWs is formally solved as

$$h_\lambda(\tau, \mathbf{k}) = \frac{4}{a(\tau)} \int^\tau d\tilde{\tau} G_{\mathbf{k}}(\tau, \tilde{\tau}) a(\tilde{\tau}) S_\lambda(\tilde{\tau}, \mathbf{k}), \quad (3.14)$$

with the Green's function  $G_{\mathbf{k}}(\tau, \tilde{\tau})$  satisfying

$$\partial_{\tilde{\tau}}^2 G_{\mathbf{k}}(\tau, \tilde{\tau}) + \left( k^2 - \frac{\partial_{\tilde{\tau}}^2 a(\tau)}{a(\tau)} \right) G_{\mathbf{k}}(\tau, \tilde{\tau}) = \delta(\tau - \tilde{\tau}). \quad (3.15)$$

It is solved as

$$G_{\mathbf{k}}(\tau, \tilde{\tau}) = \frac{\sin k(\tau - \tilde{\tau})}{k}, \quad (3.16)$$

in the RD era. Combining the above equations, the two-point function of induced GWs is given by

$$\begin{aligned} \langle h_{\lambda_1}(\tau, \mathbf{k}_1) h_{\lambda_2}(\tau, \mathbf{k}_2) \rangle &= \int \frac{d^3 q_1}{(2\pi)^3} \int \frac{d^3 q_2}{(2\pi)^3} Q_{\lambda_1}(\mathbf{k}_1, \mathbf{q}_1) Q_{\lambda_2}(\mathbf{k}_2, \mathbf{q}_2) \\ &\times I_k(|\mathbf{k}_1 - \mathbf{q}_1|, q_1, \tau) I_k(|\mathbf{k}_2 - \mathbf{q}_2|, q_2, \tau) \langle \zeta(\mathbf{q}_1) \zeta(\mathbf{k}_1 - \mathbf{q}_1) \zeta(\mathbf{q}_2) \zeta(\mathbf{k}_2 - \mathbf{q}_2) \rangle, \end{aligned} \quad (3.17)$$

with the kernel function

$$I_k(p, q, \tau) = 4 \int^\tau d\tilde{\tau} G_{\mathbf{k}}(\tau, \tilde{\tau}) \frac{a(\tilde{\tau})}{a(\tau)} f(p, q, \tilde{\tau}). \quad (3.18)$$

As we have mentioned, we calculate  $\Omega_{\text{GW}}(\tau, k)$  in the deep subhorizon limit during the RD era with  $\tau \rightarrow \infty$ , where the asymptotic form of this kernel function is simply given by

$$k\tau I_k(p, q, \tau) \underset{\tau \rightarrow \infty}{\sim} \mathcal{F}_k(p, q) [\mathcal{S}_k(p, q) \sin(k\tau) + \mathcal{C}_k(p, q) \cos(k\tau)], \quad (3.19)$$

with

$$\begin{aligned} \mathcal{F}_k(p, q) &= \frac{3(p^2 + q^2 - 3k^2)}{p^3 q^3}, \\ \mathcal{S}_k(p, q) &= -4pq + (p^2 + q^2 - 3k^2) \ln \left| \frac{3k^2 - (p+q)^2}{3k^2 - (p-q)^2} \right|, \\ \mathcal{C}_k(p, q) &= -\pi(p^2 + q^2 - 3k^2) \Theta(p + q - \sqrt{3}k). \end{aligned} \quad (3.20)$$

<sup>3</sup>Here we consider the adiabatic scalar perturbations. In the case of the isocurvature perturbations, see e.g. Ref. [95] about the transfer function.

$\Theta(x)$  is the step function. Therefore, the oscillation average of their cross-correlation reads

$$\begin{aligned} \overline{J_k^2(p_1, q_1; p_2, q_2)} &:= \lim_{\tau \rightarrow \infty} (k\tau)^2 \overline{I_k(p_1, q_1, \tau) I_k(p_2, q_2, \tau)} \\ &= \frac{1}{2} \mathcal{F}_k(p_1, q_1) \mathcal{F}_k(p_2, q_2) [\mathcal{S}_k(p_1, q_1) \mathcal{S}_k(p_2, q_2) + \mathcal{C}_k(p_1, q_2) \mathcal{C}_k(p_2, q_2)]. \end{aligned} \quad (3.21)$$

In order to evaluate the spectrum of induced GWs, we need to specify the remaining trispectrum of the primordial curvature perturbations.

### 3.2 Diagrammatic approach

Let us turn next to introduce our approach to take account of the primordial non-Gaussianity in the trispectrum of the curvature perturbations. The curvature perturbation with the local-type non-Gaussianity (i.e.,  $\zeta(\mathbf{x})$  given by some function  $\mathcal{F}_{\text{NL}}(\zeta_g(\mathbf{x}))$  of the Gaussian field  $\zeta_g(\mathbf{x})$  at the same spatial point) can be expanded in general as

$$\zeta(\mathbf{x}) = F_{\text{NL}}^{(0)} \zeta_g(\mathbf{x}) + F_{\text{NL}}^{(1)} \zeta_g^2(\mathbf{x}) + F_{\text{NL}}^{(2)} \zeta_g^3(\mathbf{x}) + F_{\text{NL}}^{(3)} \zeta_g^4(\mathbf{x}) + F_{\text{NL}}^{(4)} \zeta_g^5(\mathbf{x}) + \dots, \quad (3.22)$$

with the expansion coefficient  $F_{\text{NL}}^{(n)}$ . We assume the Gaussianity at the leading order as  $F_{\text{NL}}^{(0)} = 1$ . We also use specific characters for the first several coefficients as  $F_{\text{NL}} := F_{\text{NL}}^{(1)}$ ,  $G_{\text{NL}} := F_{\text{NL}}^{(2)}$ ,  $H_{\text{NL}} := F_{\text{NL}}^{(3)}$ ,  $I_{\text{NL}} := F_{\text{NL}}^{(4)}$ ,  $\dots$ , following the convention. Based on this expression, one can obtain the perturbative expression for the trispectrum of the curvature perturbations, and calculate the tensor power spectrum perturbatively in the power spectrum of  $\zeta_g$  (specifically in the amplitude parameter  $A_g$  given by Eq. (2.20) in our monochromatic case). As direct computations would be tedious, we employ the helpful diagrammatic approach advocated in Ref. [24] first and organized by Adshead et al. [25].

Including the transformation from the curvature perturbation to the tensor one, all the relevant Feynman rules are summarized in Fig. 3. Making use of them, we calculate the two-point function of tensor modes sourced by the scalar perturbations. That is, we first set two external tensor lines (wave lines) with the same momentum  $\mathbf{k}$  and the polarization  $\lambda$  as otherwise, the contributions will trivially vanish (see discussion in Appendix A particularly for the polarization). These two tensor lines are connected through i) the coupling  $I_k(|\mathbf{k} - \mathbf{q}|, q, \tau) Q_\lambda(\mathbf{k}, \mathbf{q})$  between one tensor  $h_\lambda(\tau, \mathbf{k})$  and two scalar curvature perturbations  $\zeta(\mathbf{k} - \mathbf{q})$  and  $\zeta(\mathbf{q})$  (dotted lines), ii) the coupling  $n! F_{\text{NL}}^{(n-1)}$  between one curvature perturbation  $\zeta(\mathbf{q}_1)$  and  $n$  Gaussian fields  $\zeta_g(\mathbf{q}_1 + \mathbf{q}_2)$ ,  $\zeta_g(\mathbf{q}_3)$ ,  $\dots$ ,  $\zeta_g(-\sum_{i=2}^n \mathbf{q}_i)$  (plane lines), satisfying the momentum conservation, and iii) the propagator  $P_g(q)$  of the Gaussian field. Then iv) one has to integrate it over each undetermined momentum  $\mathbf{q}_i$ .

The factor  $n!$  of the coupling ii) counts up all possible connections. However, one may have some loop structures such as ‘‘convolved propagators’’ and ‘‘self-closed loops’’ shown in Fig. 4, and in such a case, v) the diagram must be divided by the symmetric factor to avoid overcounts. For example, the permutation of  $n$  convolved propagators yields  $n!$  overcounts. Therefore, the symmetric factor is calculated as  $n!$  in this case. Let us also see a  $m$  self-closed loops case. The exchange of the initial and end points leads to overcount of factor 2 for each loop, and the permutation of loops themselves causes  $m!$  overcounts. In total, the symmetric factor is hence  $2^m m!$ .

For the total amplitude of GWs, all possible diagrams are summed up. We here note that loop corrections to the propagator and vertex can be formally summarized by introducing the

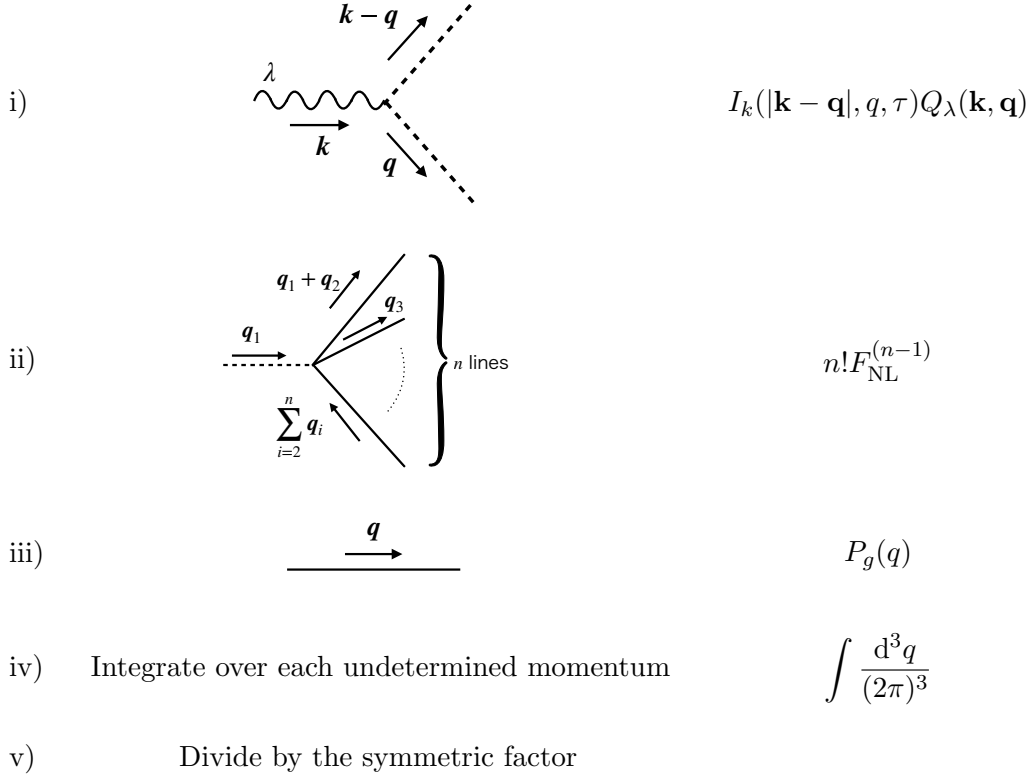


**Figure 3:** Feynman rules as the building blocks.

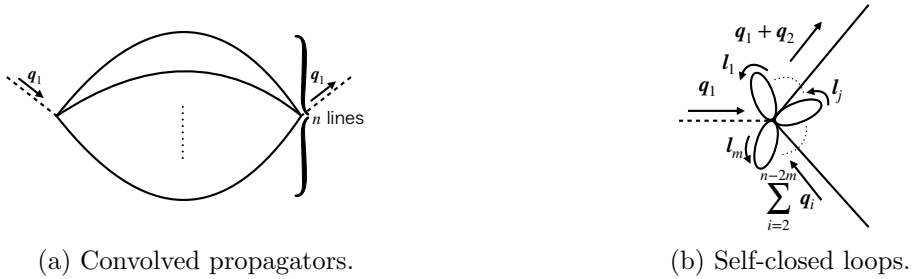


**Figure 4:** The loop structures.

“renormalized” diagrams, which are exhibited in Fig. 5. That is, we formally define the wave-plane line by the summation of convolved propagators of the Gaussian field, and the gray bubble by that of vertices with several closed loops. By replacing the plane propagator iii) and vertex ii) with these “renormalized” ones, possible loop corrections are exhausted. Note that however, the specific values of these parts depend on the number of other lines through the expansion coefficients  $F_{\text{NL}}^{(n)}$ . Therefore, the numerical contribution must be calculated for each individual diagram.

One important rule is that each curvature perturbation (dotted line), which is coupled to a tensor mode (external wave line), must be connected to another dotted line coupled to the other external wave line (tensor mode) by at least a plane line (propagator of the Gaussian field), or otherwise the diagram should include the subdiagram shown in Fig. 6.

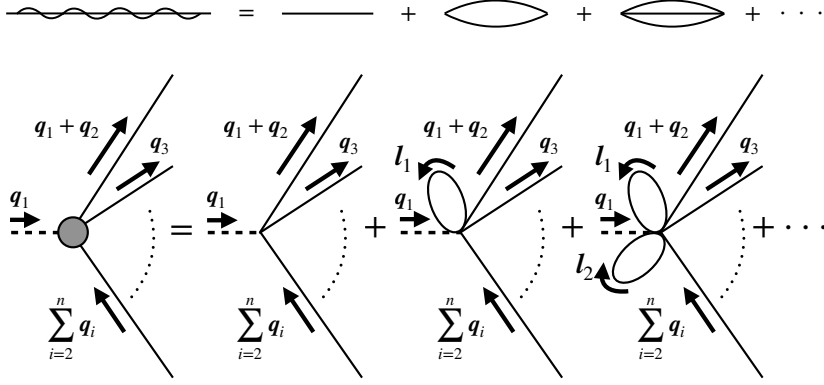


**Figure 5:** Renormalized propagator of the Gaussian field (wave-plane line) and vertex (gray bubble).

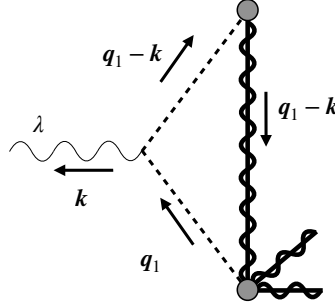


**Figure 6:** Helically prohibited subdiagram.

Based on the above Feynman rules, it is found to be proportional to

$$\begin{aligned}
& \int \frac{d^3 \mathbf{q}_1}{(2\pi)^3} Q_\lambda(\mathbf{k}, \mathbf{q}_1) f(|\mathbf{k} - \mathbf{q}_1|, q_1, \tilde{\tau}) \tilde{P}_g(q_1) \\
&= \int_0^{2\pi} d\phi \begin{cases} \cos(2\phi) & \lambda = + \\ \sin(2\phi) & \lambda = \times \end{cases} \\
& \quad \times \int \frac{q_1^2 dq_1 d\cos\theta}{(2\pi)^3} \frac{q_1^2}{\sqrt{2}} \sin^2(\theta) f\left(\sqrt{k^2 + q_1^2 - 2kq_1 \cos\theta}, q_1, \tilde{\tau}\right) \tilde{P}_g(q_1) \\
&= 0,
\end{aligned} \tag{3.23}$$

where  $\tilde{P}_g(q_1)$  can include the loop corrections. Thus, any diagram containing this subdiagram should vanish, which is due to the helicity conservation.

The minimal diagram is hence given by the left one shown in Fig. 7, which we call “Vanilla” diagram (we use the blackboard bold typeface for renormalized diagrams). Another helpful rule is that some independent diagrams in a “deformed” relation (such as “twist” and up/down or left/right “flip”) with one diagram should give the same contribution as that diagram and hence can be taken into account just by the “deformation factor”  $2^s$  ( $s = 1, 2, \text{ or } 3$ ). For example, the right diagram in Fig. 7 is independent of the left one and should be counted in. It however gives the same numerical contribution and thus we just double the left one instead of independently computing the right one. Hereafter we hence take only

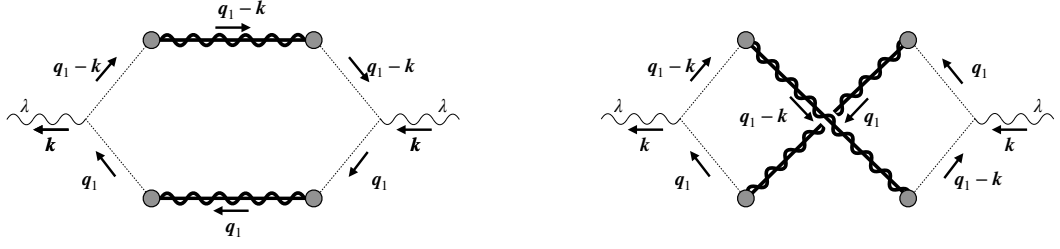


**Figure 7:** *Left:* “Vanilla” diagram as a minimal one. *Right:* the other minimal diagram, which can be taken into account just by doubling the left diagram.

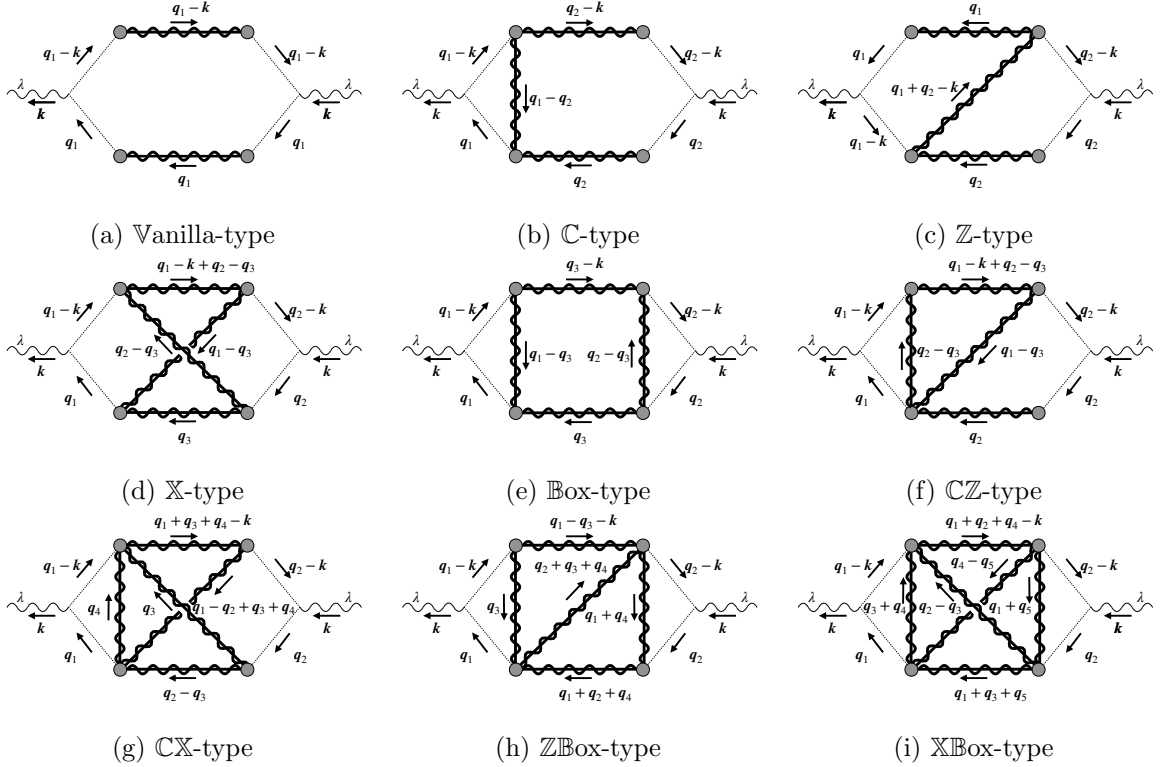


**Figure 8:** All possible contributions topologically independent.

the left one as a minimal configuration and any non-Gaussian contribution can be expressed by adding lines to this. Then all contributions can be summarized into nine topologically-independent diagrams shown in Fig. 8 because there are only four vertices in the diagram.

Finally, let us introduce a shorthand notation for the relevant integrals before moving on to the detailed calculation. We define  $\mathcal{I}_{\lambda\lambda'}$  by

$$\begin{aligned}
\mathcal{I}_{\lambda\lambda'}(\tau, \mathbf{k} \mid \mathbf{q}_1, \mathbf{q}_2 \mid \mathbf{k}_1, \mathbf{k}_2, \dots) \\
:= \int \frac{d^3 q_1}{(2\pi)^3} \frac{d^3 q_2}{(2\pi)^3} \dots Q_\lambda(\mathbf{k}, \mathbf{q}_1) Q_{\lambda'}(\mathbf{k}, \mathbf{q}_2) I_k(|\mathbf{k} - \mathbf{q}_1|, q_1, \tau) I_k(|\mathbf{k} - \mathbf{q}_2|, q_2, \tau) \\
\times P_g(k_1) P_g(k_2) \dots \quad (3.24)
\end{aligned}$$

Here  $\mathbf{k}_1, \mathbf{k}_2, \dots$  are supposed to be combinations of  $\mathbf{k}, \mathbf{q}_1, \mathbf{q}_2, \dots$ , and the integration should

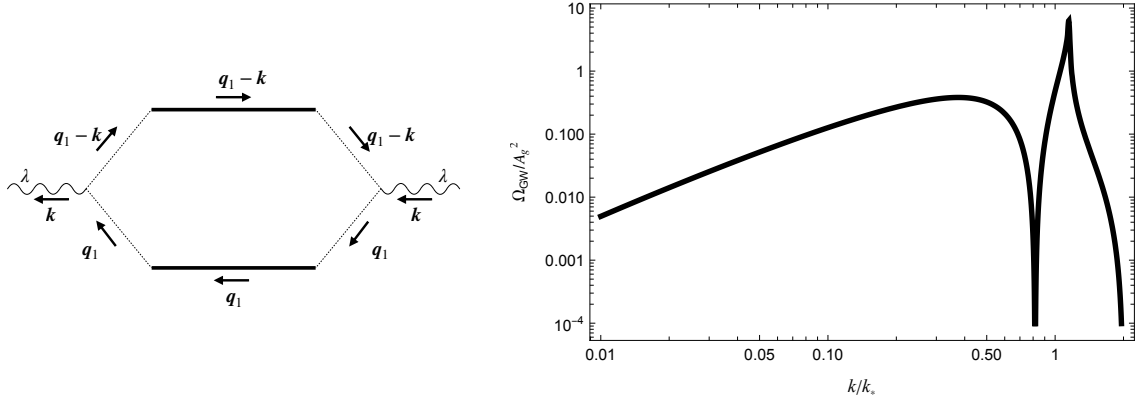


**Figure 9:** The second-order (Vanilla) contribution in a diagram (left) and the resultant normalized GW amplitude  $\Omega_{\text{GW}}^{(2)}/A_g^2$  (right).

be taken over all undetermined momenta  $\mathbf{q}_i$  ( $i = 1, 2, \dots$ ) other than  $\mathbf{k}$ . All diagrams shown below can be summarized in this integral.

### 3.2.1 Second-order contribution

Let us see specific examples order by order in our monochromatic power spectrum of the curvature perturbation (2.20). There is only one topologically-independent diagram for the leading order contribution ( $\propto A_g^2$ ), shown in the left panel of Fig. 9. Either for  $++$  or  $\times\times$  mode, this diagram reads

$$P_{\lambda\lambda}^{\text{Vanilla}}(\tau, k) = \mathcal{I}_{\lambda\lambda}(\tau, \mathbf{k} \mid \mathbf{q}, \mathbf{q} \mid \mathbf{q}, \mathbf{k} - \mathbf{q}). \quad (3.25)$$

The symmetry factor is unity because it has no loop structure, and the deformation factor is two as it can be only “twisted” (any “flip” does not yield an independent diagram). Taking account of the two polarization patterns, the amplitude of GW spectrum (3.7) then reads

$$\begin{aligned} \Omega_{\text{GW}}^{(2)}(k) &= 2^2 \times \frac{1}{48} \left( \frac{k}{aH} \right)^2 \overline{\mathcal{P}_{++}^{\text{Vanilla}}(\tau \rightarrow \infty, k)} \\ &= \frac{3A_g^2}{1024} \tilde{k}^2 \Theta(2 - \tilde{k}) (\tilde{k}^2 - 4)^2 (3\tilde{k}^2 - 2)^2 \\ &\quad \times \left( \pi^2 (3\tilde{k}^2 - 2)^2 \Theta(2\sqrt{3} - 3\tilde{k}) + \left[ 4 + (3\tilde{k}^2 - 2) \ln \left| \frac{4}{3\tilde{k}^2} - 1 \right| \right] \right), \end{aligned} \quad (3.26)$$

where  $\tilde{k} = k/k_*$ , and we used the asymptotic formula (3.21) of the kernel function  $I_k$ . The GW spectrum has a sharp peak as one can see in the right panel of Fig. 9. This is because we assume a monochromatic power spectrum.

### 3.2.2 Third-order contributions

The third-order contributions ( $\propto A_g^3$ ) are summarized in Fig. 10. The symmetric factor is unity for the C and Z terms, while it is two for the 1-convolution term and 1-loop term.



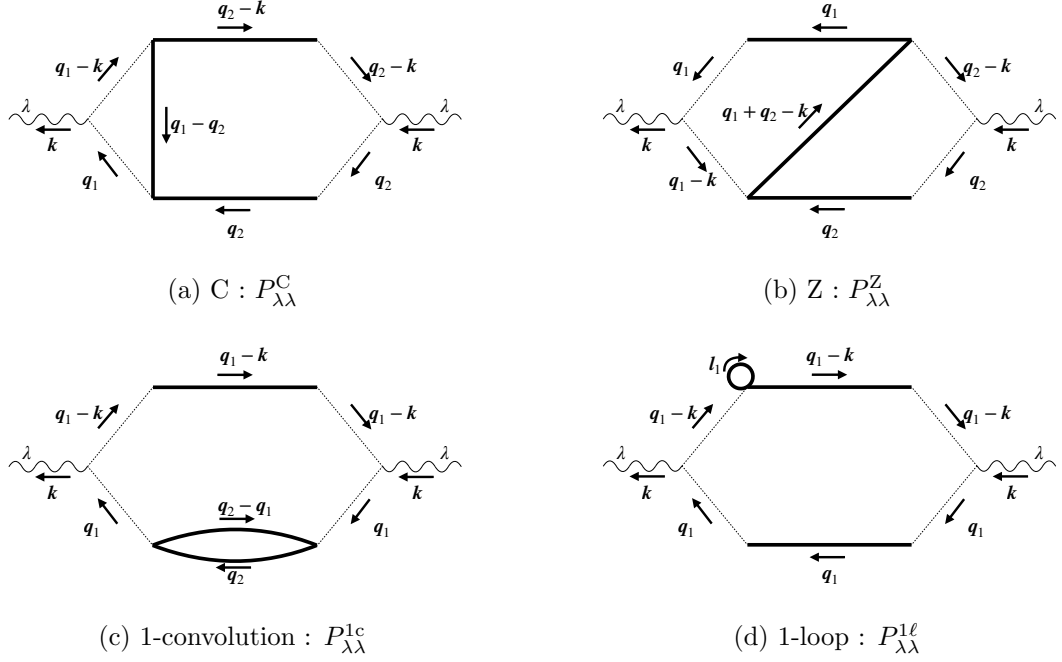


**Figure 10:** Third-order contributions.

Hence they are summarized as

$$\begin{aligned}
P_{\lambda\lambda}^C(\tau, k) &= (2!F_{\text{NL}})^2 \mathcal{I}_{\lambda\lambda}(\tau, \mathbf{k} \mid \mathbf{q}_1, \mathbf{q}_2 \mid \mathbf{q}_2, \mathbf{k} - \mathbf{q}_2, \mathbf{q}_1 - \mathbf{q}_2), \\
P_{\lambda\lambda}^Z(\tau, k) &= (2!F_{\text{NL}})^2 \mathcal{I}_{\lambda\lambda}(\tau, \mathbf{k} \mid \mathbf{q}_1, \mathbf{q}_2 \mid \mathbf{q}_1, \mathbf{q}_2, \mathbf{k} - \mathbf{q}_1 - \mathbf{q}_2), \\
P_{\lambda\lambda}^{1c}(\tau, k) &= \frac{(2!F_{\text{NL}})^2}{2!} \mathcal{I}_{\lambda\lambda}(\tau, \mathbf{k} \mid \mathbf{q}_1, \mathbf{q}_1 \mid \mathbf{k} - \mathbf{q}_1, \mathbf{q}_2, \mathbf{q}_1 - \mathbf{q}_2), \\
P_{\lambda\lambda}^{1\ell}(\tau, k) &= \left( \frac{3!G_{\text{NL}}}{2!} \int \frac{d^3 l_1}{(2\pi)^3} P_g(l_1) \right) P_{\lambda\lambda}^{\text{Vanilla}}(k) = 3G_{\text{NL}} A_g P_{\lambda\lambda}^{\text{Vanilla}}.
\end{aligned} \tag{3.27}$$

One finds in the 1-loop term that adding self-closed loops to some diagram can be practically realized by multiplying the original diagram by the expansion coefficients and the perturbation amplitude  $A_g$ .

The deformation factors read  $2^2$  for the C, Z, and 1-convolution terms and  $2^3$  for the 1-loop term. Therefore, the third-order GW spectrum is given by

$$\Omega_{\text{GW}}^{(3)}(k) = 2 \times \frac{1}{48} \left( \frac{k}{aH} \right)^2 \left[ 2^2 \times \overline{\mathcal{P}_{++}^C}(k) + 2^2 \times \overline{\mathcal{P}_{++}^Z}(k) + 2^2 \times \overline{\mathcal{P}_{++}^{1c}}(k) + 2^3 \times \overline{\mathcal{P}_{++}^{1\ell}}(k) \right]. \tag{3.28}$$

Though the integrations cannot be done analytically in contrast to the Vanilla case (3.26), we show the numerical results in Fig. 11, which include two polarizations and the deformation factors. We do not explicitly show the 1-loop term because it is just a constant multiplication of the Vanilla term shown in Fig. 9.

### 3.2.3 Fourth-order contributions

Fourth-order contributions ( $\propto A_g^4$ ) are summarized in Figs. 12 and 13. (1,1)-conv, Box, and X terms have been provided in [25] and 2-conv term has been introduced by [26], while

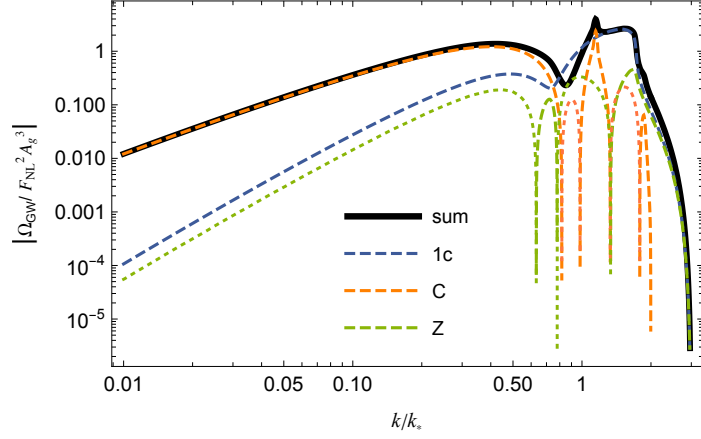


**Figure 11:** The normalized GW amplitude of third-order contributions except for the 1-loop term, which is just a constant multiplication of the Vanilla term shown in Fig. 9. We represent the third-order total amplitude as the black solid line. Dashed and dotted lines respectively show where the sign of  $\Omega_{\text{GW}}$  is positive and negative. We note that this plot is including two polarizations and the deformation factors.

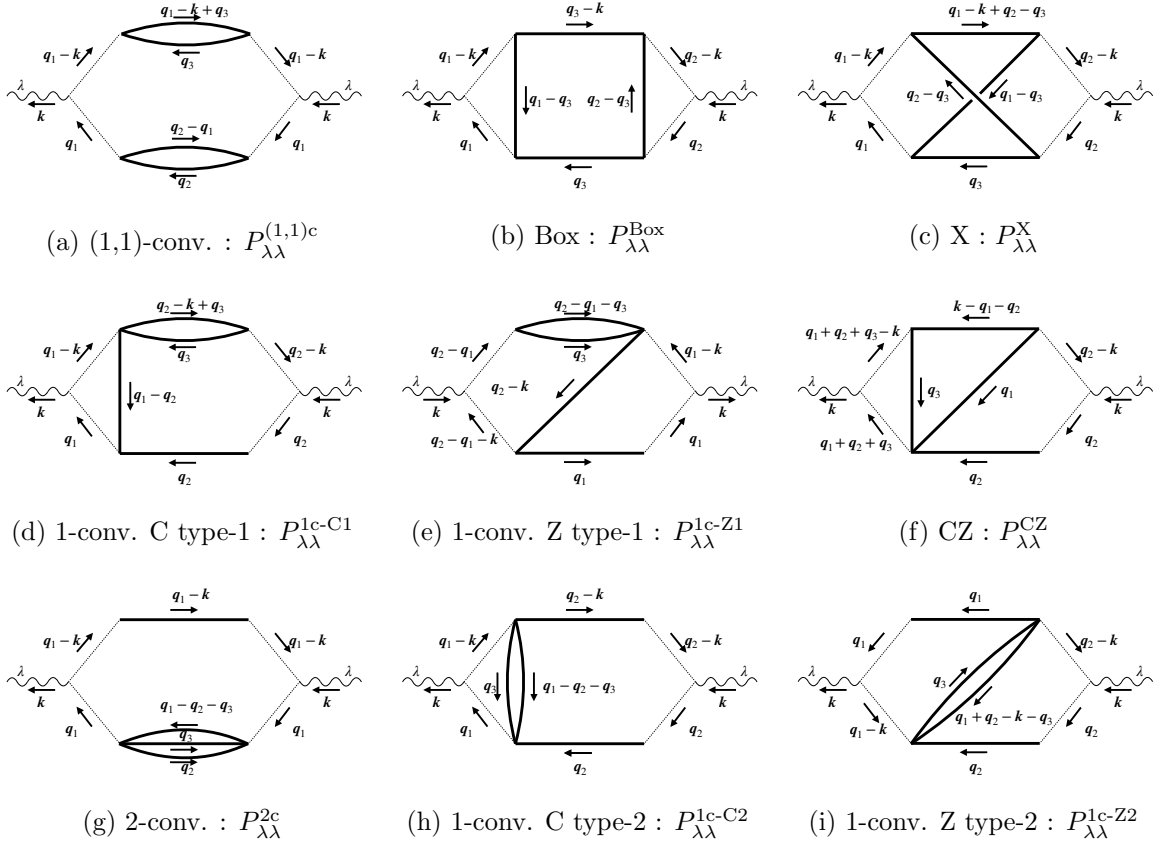


**Figure 12:** Fourth-order contributions without self-closed loops.

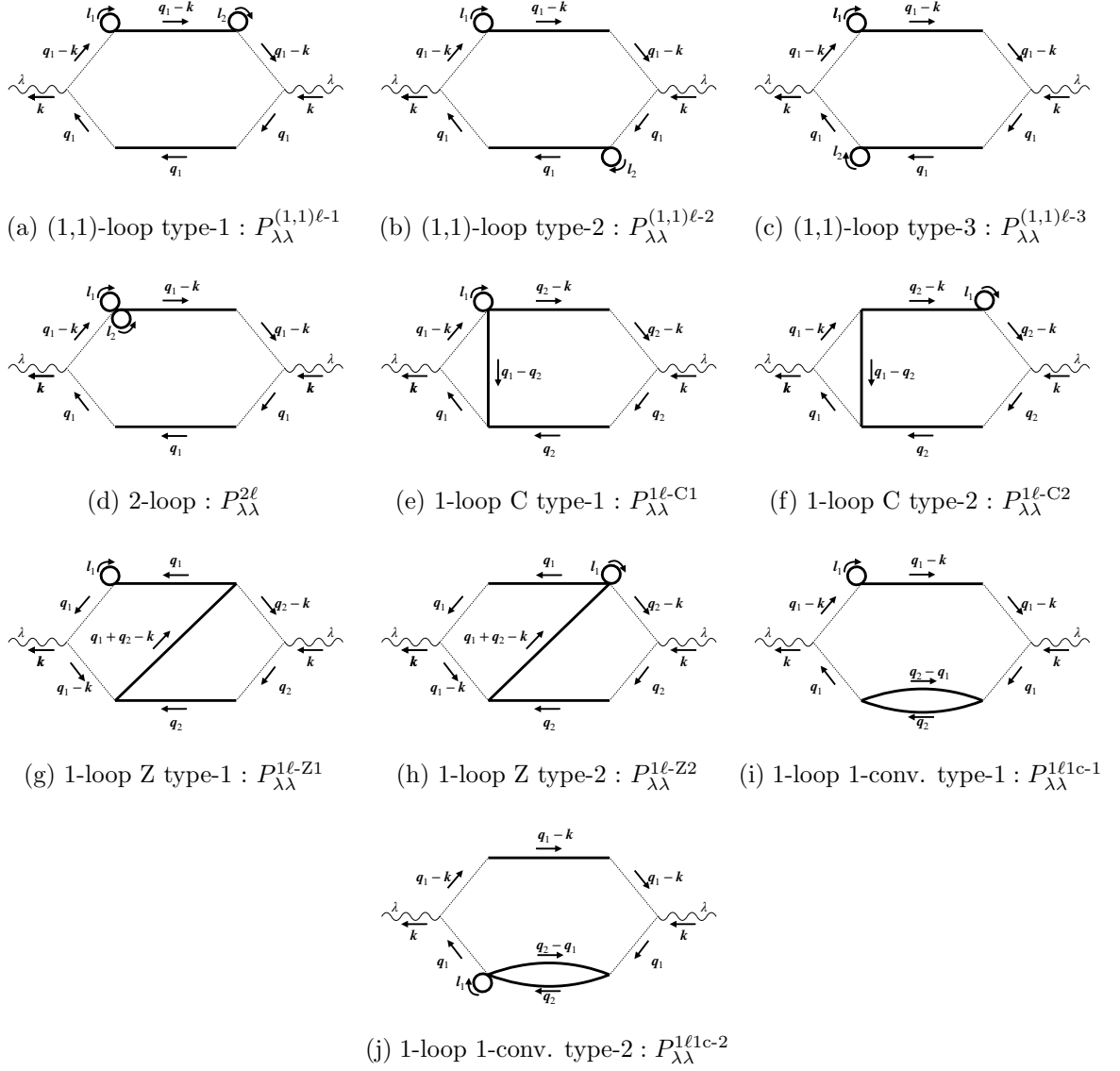


**Figure 13:** Fourteenth-order contributions with self-closed loops.

other contributions in Fig. 12 and all contributions in Fig. 13 are our new findings. They read

$$\begin{aligned}
P_{\lambda\lambda}^{(1,1)c}(\tau, k) &= \frac{(2!F_{\text{NL}})^4}{(2!)^2} \mathcal{I}_{\lambda\lambda}(\tau, \mathbf{k} \mid \mathbf{q}_1, \mathbf{q}_1 \mid \mathbf{q}_1 - \mathbf{k} + \mathbf{q}_3, \mathbf{q}_3, \mathbf{q}_2, \mathbf{q}_2 - \mathbf{q}_1), \\
P_{\lambda\lambda}^{\text{Box}}(\tau, k) &= (2!F_{\text{NL}})^4 \mathcal{I}_{\lambda\lambda}(\tau, \mathbf{k} \mid \mathbf{q}_1, \mathbf{q}_2 \mid \mathbf{q}_1 - \mathbf{q}_3, \mathbf{q}_2 - \mathbf{q}_3, \mathbf{q}_3, \mathbf{q}_3 - \mathbf{k}), \\
P_{\lambda\lambda}^{\text{X}}(\tau, k) &= (2!F_{\text{NL}})^4 \mathcal{I}_{\lambda\lambda}(\tau, \mathbf{k} \mid \mathbf{q}_1, \mathbf{q}_2 \mid \mathbf{q}_1 - \mathbf{k} + \mathbf{q}_2 - \mathbf{q}_3, \mathbf{q}_1 - \mathbf{q}_3, \mathbf{q}_2 - \mathbf{q}_3, \mathbf{q}_3),
\end{aligned} \tag{3.29}$$

for ones proportional to  $F_{\text{NL}}^4$ ,

$$\begin{aligned}
P_{\lambda\lambda}^{1c-C1}(\tau, k) &= \frac{(2!F_{\text{NL}})^2 3!G_{\text{NL}}}{2!} \mathcal{I}_{\lambda\lambda}(\tau, \mathbf{k} \mid \mathbf{q}_1, \mathbf{q}_2 \mid \mathbf{q}_1 - \mathbf{q}_2, \mathbf{q}_2, \mathbf{q}_3, \mathbf{q}_2 - \mathbf{k} + \mathbf{q}_3), \\
P_{\lambda\lambda}^{1c-Z1}(\tau, k) &= \frac{(2!F_{\text{NL}})^2 3!G_{\text{NL}}}{2!} \mathcal{I}_{\lambda\lambda}(\tau, \mathbf{k} \mid \mathbf{q}_1, \mathbf{q}_2 - \mathbf{q}_1 \mid \mathbf{q}_1, \mathbf{q}_2 - \mathbf{k}, \mathbf{q}_3, \mathbf{q}_2 - \mathbf{q}_1 - \mathbf{q}_3), \\
P_{\lambda\lambda}^{\text{CZ}}(\tau, k) &= (2!F_{\text{NL}})^2 3!G_{\text{NL}} \mathcal{I}_{\lambda\lambda}(\tau, \mathbf{k} \mid \mathbf{q}_1 + \mathbf{q}_2 + \mathbf{q}_3, \mathbf{q}_2 \mid \mathbf{q}_1, \mathbf{q}_2, \mathbf{q}_3, \mathbf{k} - \mathbf{q}_1 - \mathbf{q}_2),
\end{aligned} \tag{3.30}$$

for ones proportional to  $F_{\text{NL}}^2 G_{\text{NL}}$ ,<sup>4</sup>

$$\begin{aligned}
P_{\lambda\lambda}^{2c}(\tau, k) &= \frac{(3!G_{\text{NL}})^2}{3!} \mathcal{I}_{\lambda\lambda}(\tau, \mathbf{k} \mid \mathbf{q}_1, \mathbf{q}_2 \mid \mathbf{k} - \mathbf{q}_1, \mathbf{q}_2, \mathbf{q}_3, \mathbf{q}_1 - \mathbf{q}_2 - \mathbf{q}_3), \\
P_{\lambda\lambda}^{1c-C2}(\tau, k) &= \frac{(3!G_{\text{NL}})^2}{2!} \mathcal{I}_{\lambda\lambda}(\tau, \mathbf{k} \mid \mathbf{q}_1, \mathbf{q}_2 \mid \mathbf{q}_1 - \mathbf{q}_2 - \mathbf{q}_3, \mathbf{q}_2, \mathbf{q}_3, \mathbf{q}_2 - \mathbf{k}), \\
P_{\lambda\lambda}^{1c-Z2}(\tau, k) &= \frac{(3!G_{\text{NL}})^2}{2!} \mathcal{I}_{\lambda\lambda}(\tau, \mathbf{k} \mid \mathbf{q}_1, \mathbf{q}_2 \mid \mathbf{q}_1, \mathbf{q}_2, \mathbf{q}_3, \mathbf{q}_1 + \mathbf{q}_2 - \mathbf{k} - \mathbf{q}_3),
\end{aligned} \tag{3.31}$$

for ones proportional to  $G_{\text{NL}}^2$  (above nine diagrams are shown in Fig. 12), and

$$\begin{aligned}
P_{\lambda\lambda}^{(1,1)\ell-1}(\tau, k) &= P_{\lambda\lambda}^{(1,1)\ell-2}(\tau, k) = P_{\lambda\lambda}^{(1,1)\ell-3}(\tau, k) = \frac{(3!G_{\text{NL}})^2}{(2!)^2} A_g^2 P_{\lambda\lambda}^{\text{Vanilla}}(\tau, k), \\
P_{\lambda\lambda}^{2\ell}(\tau, k) &= \frac{5!I_{\text{NL}}}{2^2 2!} A_g^2 P_{\lambda\lambda}^{\text{Vanilla}}(\tau, k), \quad P_{\lambda\lambda}^{1\ell-C1}(\tau, k) = \frac{4!H_{\text{NL}}}{2!} \frac{A_g P_{\lambda\lambda}^{\text{C}}(\tau, k)}{2!F_{\text{NL}}}, \\
P_{\lambda\lambda}^{1\ell-C2}(\tau, k) &= \frac{3!G_{\text{NL}}}{2!} A_g P_{\lambda\lambda}^{\text{C}}(\tau, k), \quad P_{\lambda\lambda}^{1\ell-Z1}(\tau, k) = \frac{3!G_{\text{NL}}}{2!} A_g P_{\lambda\lambda}^{\text{Z}}(\tau, k), \\
P_{\lambda\lambda}^{1\ell-Z2}(\tau, k) &= \frac{4!H_{\text{NL}}}{2!} \frac{A_g P_{\lambda\lambda}^{\text{Z}}(\tau, k)}{2!F_{\text{NL}}}, \quad P_{\lambda\lambda}^{1\ell 1c-1}(\tau, k) = \frac{3!G_{\text{NL}}}{2!} A_g P_{\lambda\lambda}^{1c}(\tau, k), \\
P_{\lambda\lambda}^{1\ell 1c-2}(\tau, k) &= \frac{4!H_{\text{NL}}}{2!} \frac{A_g P_{\lambda\lambda}^{1c}(\tau, k)}{2!F_{\text{NL}}},
\end{aligned} \tag{3.32}$$

for ones including self-closed loops shown in Fig. 13. Fourth-order diagrams basically include highly multi-dimensional integrals and their specific computations require several techniques. Particularly for the 1-convolution C (1c-C1 and 1c-C2), 1-convolution Z (1c-Z1 and 1c-Z2), and CZ terms, we describe the detailed calculations in Appendix A.

Including the deformation factors, the GW spectrum is summarized as

$$\begin{aligned}
\Omega_{\text{GW}}^{(4)}(k) &= \frac{2}{48} \left( \frac{k}{aH} \right)^2 \left[ \overline{2\mathcal{P}_{++}^{(1,1)c}(k)} + \overline{2\mathcal{P}_{++}^{\text{Box}}(k)} + \overline{\mathcal{P}_{++}^{\text{X}}(k)} + \overline{2^3\mathcal{P}_{++}^{1c-C1}(k)} + \overline{2^3\mathcal{P}_{++}^{1c-Z1}(k)} \right. \\
&\quad + \overline{2^3\mathcal{P}_{++}^{\text{CZ}}(k)} + \overline{2^2\mathcal{P}_{++}^{2c}(k)} + \overline{2^2\mathcal{P}_{++}^{1c-C2}(k)} + \overline{2\mathcal{P}_{++}^{1c-Z2}(k)} + 3 \times \overline{2^2\mathcal{P}_{++}^{(1,1)\ell}(k)} + \overline{2^3\mathcal{P}_{++}^{2\ell}(k)} \\
&\quad \left. + \overline{2^3\mathcal{P}_{++}^{1\ell-C1}(k)} + \overline{2^3\mathcal{P}_{++}^{1\ell-C2}(k)} + \overline{2^3\mathcal{P}_{++}^{1\ell-Z1}(k)} + \overline{2^3\mathcal{P}_{++}^{1\ell-Z2}(k)} + \overline{2^3\mathcal{P}_{++}^{1\ell 1c-1}(k)} + \overline{2^3\mathcal{P}_{++}^{1\ell 1c-2}(k)} \right].
\end{aligned} \tag{3.33}$$

The numerical results are shown in Fig. 14. Again we do not show the contributions with self-closed loops because they are constant multiplications of lower-order diagrams.

<sup>4</sup>Here we note that for the 1c-Z1 and CZ terms the assignment of  $\mathbf{q}_1$  and  $\mathbf{q}_2$  in the diagram are different from those for the other terms, which is just for the computational reason (see Appendix A).

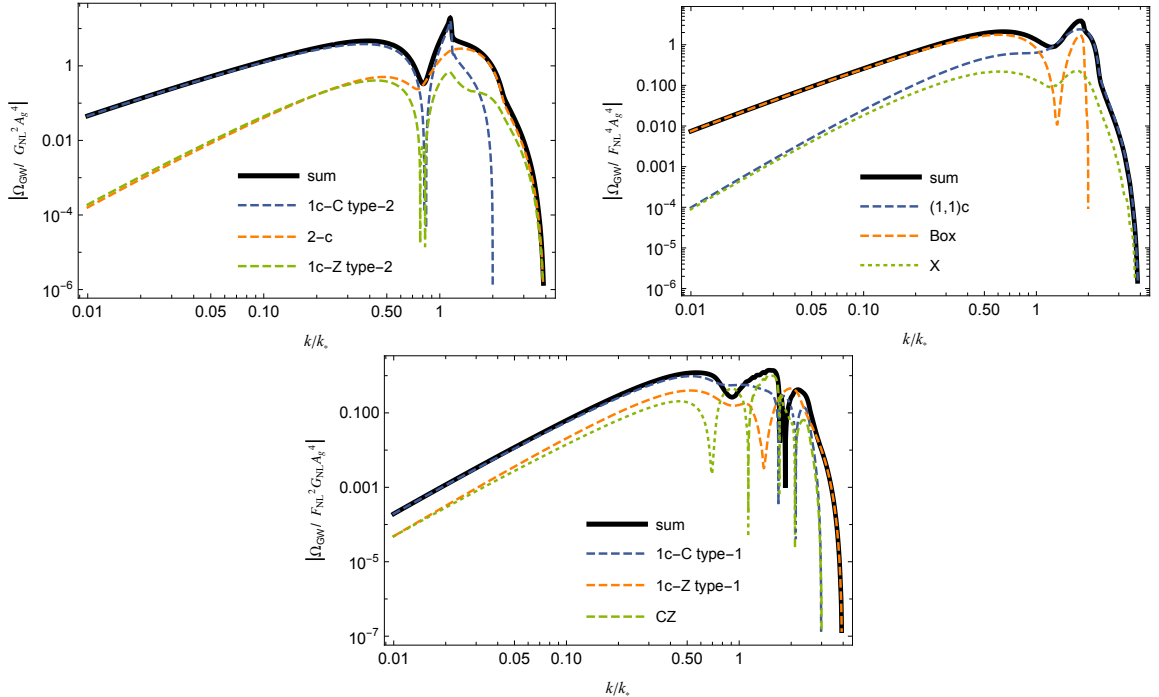


**Figure 14:** The normalized GW amplitude of fourth-order contributions except for ones with self-closed loops. In each figure, we represent the fourth-order total amplitude as the black solid line. The dashed and dotted lines show the spectrum of  $\Omega_{\text{GW}}$  where the sign is positive and negative respectively. The high-frequency side of the X term is wavering, which is due to numerical error. We note that these plots are including two polarizations and the deformation factors.

#### 4 Application to the exponential tail case

Having been armed with all weapons, we here show the scalar-induced GWs spectrum associated with PBH DM in the exponential tail case. The explicit expansion of the exponential tail mapping (2.5) first specifies the expansion coefficients (3.22) as  $F_{\text{NL}} = 3/2$ ,  $G_{\text{NL}} = 3$ ,  $H_{\text{NL}} = 27/4$ ,  $I_{\text{NL}} = 81/5$ , etc. We fix the perturbation amplitude  $A_g$  and the peak scale  $k_*$  as  $A_g = 1.32 \times 10^{-3}$  and  $k_* = 1.56 \times 10^{-12} \text{ Mpc}^{-1}$  similarly to Sec. 2. PBHs account for the full DM abundance around  $M \sim 10^{22} \text{ g}$  in this case as shown in Fig. 2. The corresponding induced GW spectrum is then shown in Fig. 15 in terms of its frequency  $f = k/(2\pi)$ . We first confirm that the leading order Vanilla contribution  $\sim \mathcal{O}(A_g^2)$  is dominant and the series expansion of the GW spectrum soon converges due to the smallness of  $A_g$  even in the non-perturbative exponential-tail non-Gaussianity case as expected in the previous section. The leading order contribution is enough for the LISA's sensitivity and it would hold true if one includes the higher order corrections in the gravitational potential  $\Phi$  which we mentioned in footnote 2 because the nonlinearity parameters due to gravity are expected to be order-unity. The leading order one is simply proportional to  $A_g^2$  and thus the GW amplitude is reduced by  $\left(\frac{1.32 \times 10^{-3}}{5.17 \times 10^{-3}}\right)^2 \simeq 0.065$  compared with the case where  $\zeta$  is purely Gaussian (recall that  $A_g = 5.17 \times 10^{-3}$  is required for  $f_{\text{PBH}} = 1$  in the Gaussian case as shown in Fig. 1). The induced GW can still be detected by LISA thanks to its high sensitivity. Note that the

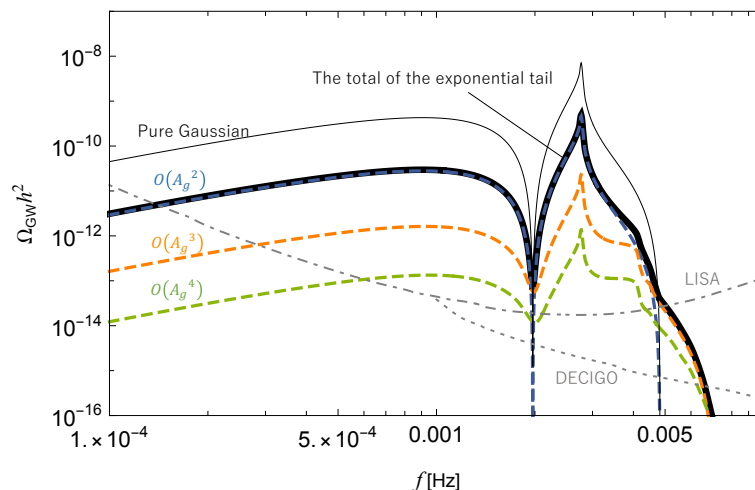


**Figure 15:** The prediction of the current induced GW spectrum associated with the PBH DM scenario shown in Fig. 2 in the exponential tail case (black thick line). Contributions of  $\mathcal{O}(A_g^2)$ ,  $\mathcal{O}(A_g^3)$ , and  $\mathcal{O}(A_g^4)$  are shown by blue-dashed, orange-dashed, and green-dashed lines, respectively. The leading contribution  $\sim \mathcal{O}(A_g^2)$  is dominant even in the non-perturbative exponential tail case because of the smallness of  $A_g$  ( $= 1.32 \times 10^{-3}$ ). As a comparison, the black thin line shows the prediction for  $f_{\text{PBH}} = 1$  if the primordial curvature perturbation is purely Gaussian with the same peak scale  $k_* = 1.56 \times 10^{-12} \text{ Mpc}^{-1}$ . The expected GW amplitude is reduced by  $\sim \left(\frac{1.32 \times 10^{-3}}{5.17 \times 10^{-3}}\right)^2 \simeq 0.065$  in the exponential tail case because the required primordial amplitude  $A_g$  is reduced from  $5.17 \times 10^{-3}$  to  $1.32 \times 10^{-3}$ . Nevertheless, it is still detectable by LISA, whose sensitivity is illustrated by the gray dot-dashed line. Deeper observations such as DECIGO shown by the gray-dotted line may distinguish the non-Gaussian signature in the high-frequency tail, though it requires more thorough investigations (see the text). Both sensitivities are taken from Ref. [96].

perturbation amplitude  $A_g$  and hence the GW amplitude are really insensitive to the small change of  $f_{\text{PBH}}$  as shown in Fig. 1. Fixing the amplitude  $A_g$  by the requirement of  $f_{\text{PBH}}^{\text{tot}} = 1$  then it could be said that the typical amplitude of induced GWs is determined by the non-Gaussian nature of the primordial perturbation. We also note that the relation between the PBH mass and the GW frequency does not change so much due to the non-Gaussianity (see Ref. [1]) but is almost determined through the mass-scale relation (2.22).

## 5 Conclusions

The scalar-induced stochastic GWs accompanying the enhanced primordial fluctuations to form the PBHs is one of the probes to test the PBH DM model. In this work, we have investigated the induced GW spectrum associated with the model where the primordial curvature perturbations have the exponential-tail non-Gaussian distribution.

We first review the PBH abundance prediction with the exponential-tail non-Gaussianity in Sec. 2, following Ref. [1]. In Sec. 3, we then extend the formulation of the two-point function of the GWs induced by the second-order scalar perturbations to the case where the primordial curvature perturbations show the general local-type non-Gaussianity. To take account of the non-Gaussian corrections into the trispectrum of the curvature perturbation,

we have employed the diagrammatic approach developed in Refs. [24, 25]. The minimal configuration is represented by the “Vanilla” diagram shown in Fig. 7, and any non-Gaussian contribution can be represented by adding lines to this “Vanilla” diagram. We found that all non-Gaussian contributions can be summarized into nine topologically-independent diagrams shown in Fig. 8.

In Sec. 4, we have adopted this general formalism to the exponential-tail-type curvature perturbations in the model where PBHs with the mass of  $10^{22}$  g are whole DM. We calculated the scalar-induced GW spectrum with the non-Gaussian contributions up to the fourth order in terms of the amplitude parameter for the Gaussian field of the curvature perturbations,  $A_g$ . Even though the non-perturbative nature of the exponential tail is crucial for the PBH abundance, the GW amplitude is well given by the leading order contribution  $\sim \mathcal{O}(A_g^2)$  thanks to the smallness of  $A_g = 1.32 \times 10^{-3}$ . The expected GW amplitude is reduced by  $\left(\frac{1.32 \times 10^{-3}}{5.17 \times 10^{-3}}\right)^2 \simeq 0.065$  compared with the pure Gaussian case, but it is still large enough to be detected by LISA.

It is worth mentioning that the non-Gaussian contributions can appear on the high-frequency side. This is because, while the leading term can produce GWs only up to  $k = 2k_*$  due to the momentum conservation, higher order terms can go beyond that through more complicated momentum configurations. Though they cannot be distinguished in the LISA’s sensitivity, it might be possible to obtain information about the primordial non-Gaussianity from GW observation with deeper sensitivity such as DECIGO, although the precise spectrum would depend on the UV behavior of the power spectrum of the curvature perturbation [27]. The enhancement of the primordial power spectrum induced by the ultra slow-roll models requires a typical width being broad [97]. Although we simply analyzed the Dirac delta function, in practice, it needs to take an effect of some finite width into account for the evaluation of the GWs spectrum. One also has to include gravitational higher-order corrections such as  $h \sim \Phi^3, \Phi^4, \dots$  which we have neglected in this work [90–92]. Gauge issues [78–89] would be relevant, too. We leave this possibility for future works.

## Acknowledgments

This work is supported by JST FOREST Program JPMJFR20352935 (R.I.) and JSPS KAKENHI Grants No. JP20J22260 (K.T.A.), No. JP21K13918 (Y.T.), No. JP20H01932 (S.Y.), and No. JP20K03968 (S.Y.).

## A Detailed computations for fourth-order diagrams

### A.1 1-convolution C term

The explicit expressions of 1c-C1 and 1c-C2 terms are given by

$$\begin{aligned}
P_{\lambda\lambda'}^{1c-C1}(\tau, k) &= \frac{(2!F_{\text{NL}})^2 3!G_{\text{NL}}}{2!} \int \frac{d^3q_1}{(2\pi)^3} \frac{d^3q_2}{(2\pi)^3} \frac{d^3q_3}{(2\pi)^3} Q_\lambda(\mathbf{k}, \mathbf{q}_1) Q_{\lambda'}(\mathbf{k}, \mathbf{q}_2) \\
&\quad \times I_k(|\mathbf{k} - \mathbf{q}_1|, q_1, \tau) I_k(|\mathbf{k} - \mathbf{q}_2|, q_2, \tau) P_g(q_2) P_g(|\mathbf{k} - \mathbf{q}_2 - \mathbf{q}_3|) P_g(q_3) P_g(|\mathbf{q}_1 - \mathbf{q}_2|), \\
P_{\lambda\lambda'}^{1c-C2}(\tau, k) &= \frac{(3!G_{\text{NL}})^2}{2!} \int \frac{d^3q_1}{(2\pi)^3} \frac{d^3q_2}{(2\pi)^3} \frac{d^3q_3}{(2\pi)^3} Q_\lambda(\mathbf{k}, \mathbf{q}_1) Q_{\lambda'}(\mathbf{k}, \mathbf{q}_2) \\
&\quad \times I_k(|\mathbf{k} - \mathbf{q}_1|, q_1, \tau) I_k(|\mathbf{k} - \mathbf{q}_2|, q_2, \tau) P_g(q_2) P_g(|\mathbf{k} - \mathbf{q}_2|) P_g(q_3) P_g(|\mathbf{q}_1 - \mathbf{q}_2 - \mathbf{q}_3|).
\end{aligned} \tag{A.1}$$

We hereafter allow different polarizations for  $\lambda$  and  $\lambda'$ . Under the monochromatic assumption (2.20),

$$P_g = \frac{2\pi^2}{k^3} A_g \delta(\ln k - \ln k_*), \quad (\text{A.2})$$

these multiple integrations are simplified to some extent.

First of all, the convolved propagator part ( $\mathbf{q}_3$  integral) can be calculated as the following formula,

$$\int \frac{d^3 q}{(2\pi)^3} P_g(q) P_g(|\mathbf{k} - \mathbf{q}|) = \frac{\pi^2 A_g^2}{k k_*^2} \Theta(2k_* - k). \quad (\text{A.3})$$

For the 1c-C1 term, the remaining momentum constraints are rewritten as

$$\delta(\ln |\mathbf{q}_1 - \mathbf{q}_2| - \ln k_*) \delta(\ln q_2 - \ln k_*) = \frac{2k_*^2}{q_{1*}^2} \delta(\ln q_1 - \ln q_{1*}) \delta(\ln q_2 - \ln k_*), \quad (\text{A.4})$$

where

$$q_{1*} = 2k_*(\sin \theta_1 \sin \theta_2 \cos(\phi_1 - \phi_2) + \cos \theta_1 \cos \theta_2), \quad (\text{A.5})$$

in the polar coordinate expression  $\mathbf{q}_i = q_i(\sin \theta_i \cos \phi_i, \sin \theta_i \sin \phi_i, \cos \theta_i)$ . Accordingly, the (dimensionless) power spectrum for the 1c-C1 term reduces to

$$\begin{aligned} \mathcal{P}_{\lambda\lambda'}^{1\text{c-C1}}(\tau, k) &= \frac{3F_{\text{NL}}^2 G_{\text{NL}} A_g^4 k^3}{4\pi^2 k_*^3} \int d \cos \theta_1 d \phi_1 d \cos \theta_2 d \phi_2 Q_\lambda(\mathbf{k}, \mathbf{q}_1) Q_{\lambda'}(\mathbf{k}, \mathbf{q}_2) \\ &\times I_k(|\mathbf{k} - \mathbf{q}_1|, q_1, \tau) I_k(|\mathbf{k} - \mathbf{q}_2|, q_2, \tau) \frac{q_1}{|\mathbf{k} - \mathbf{q}_2|} \Theta(2k_* - |\mathbf{k} - \mathbf{q}_2|) \Big|_{q_1=q_{1*}, q_2=k_*}. \end{aligned} \quad (\text{A.6})$$

Changing the integration variables from  $\phi_1$  and  $\phi_2$  to  $\varphi = \phi_1 - \phi_2$  and  $\phi_2$ , one finds that the second line does not depend on  $\phi_2$ . Therefore, the  $\phi_2$  integration can be summarized in the polarization part as

$$\begin{aligned} Q_{\lambda\lambda'}^2(\mathbf{k}, \mathbf{q}_1, \mathbf{q}_2) &:= \int d \phi_2 Q_\lambda(\mathbf{k}, \mathbf{q}_1) Q_{\lambda'}(\mathbf{k}, \mathbf{q}_2) \\ &= \frac{q_1^2 q_2^2 \pi}{2} \sin^2 \theta_1 \sin^2 \theta_2 \times \begin{cases} \cos(2\varphi) & \text{for } \lambda = \lambda', \\ \sin(2\varphi) & \text{for } \lambda = \times \text{ and } \lambda' = +, \\ -\sin(2\varphi) & \text{for } \lambda = + \text{ and } \lambda' = \times. \end{cases} \end{aligned} \quad (\text{A.7})$$

Including the deformation factor  $2^3$  for the 1c-C1 term, the corresponding GW density parameter reads

$$\begin{aligned} \Omega_{\lambda\lambda'}^{1\text{c-C1}}(k) &= \lim_{\tau \rightarrow \infty} \frac{2^3}{48} (k\tau)^2 \overline{\mathcal{P}_{\lambda\lambda'}^{1\text{c-C1}}(\tau, k)} \\ &= \frac{F_{\text{NL}}^2 G_{\text{NL}} A_g^4 k^3}{8\pi^2 k_*^3} \int d \cos \theta_1 d \cos \theta_2 d \varphi Q_{\lambda\lambda'}^2(\mathbf{k}, \mathbf{q}_1, \mathbf{q}_2) \\ &\times \overline{J_k^2(|\mathbf{k} - \mathbf{q}_1|, q_1; |\mathbf{k} - \mathbf{q}_2|, q_2)} \frac{q_1}{|\mathbf{k} - \mathbf{q}_2|} \Theta(2k_* - |\mathbf{k} - \mathbf{q}_2|) \Big|_{q_1=q_{1*}, q_2=k_*}. \end{aligned} \quad (\text{A.8})$$



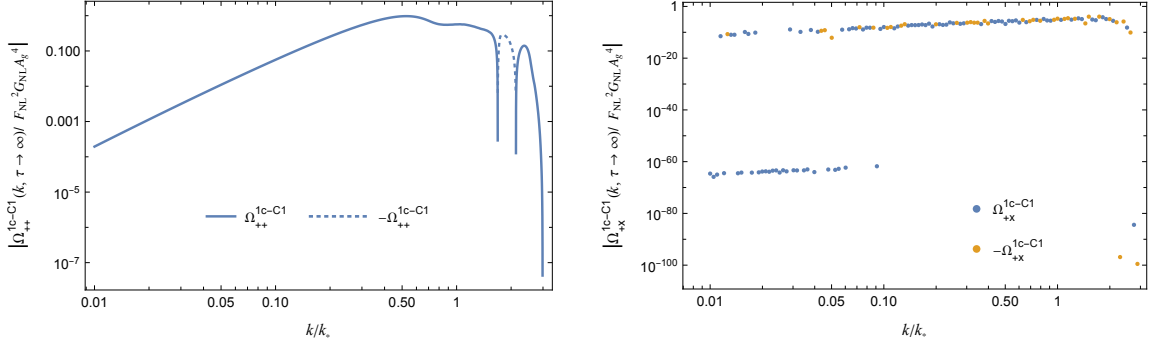


**Figure 16:** The normalized GW amplitudes  $|\Omega_{++}^{1c-C1}/F_{\text{NL}}^2 G_{\text{NL}} A_g^4|$  (left) and  $|\Omega_{xx}^{1c-C1}/F_{\text{NL}}^2 G_{\text{NL}} A_g^4|$  (right). The plane and dotted lines are for positive and negative values respectively in the left panel, while the blue and orange points are for positive and negative in the right panel.

The numerical result of this integral is shown in Fig. 16. One finds that the GW amplitude indeed vanishes for  $\lambda \neq \lambda'$  within the numerical error.

For the 1c-C2 term, the remaining constraints after the  $\mathbf{q}_3$  integral are rewritten as

$$\delta(\ln q_2 - \ln k_*) \delta(\ln |\mathbf{k} - \mathbf{q}_2| - \ln k_*) = \frac{k_*}{k} \delta(\ln q_2 - \ln k_*) \delta(\cos \theta_2 - \mu_{2*}), \quad (\text{A.9})$$

where  $\mu_{2*} = k/(2k_*)$ . The corresponding power spectrum then reads

$$\begin{aligned} \mathcal{P}_{\lambda\lambda'}^{1c-C2}(\tau, k) &= \frac{9G_{\text{NL}}^2 A_g^4 k^2}{16\pi^2 k_*^4} \int dq_1 d\cos\theta_1 d\varphi Q_{\lambda\lambda'}^2(\mathbf{k}, \mathbf{q}_1, \mathbf{q}_2) \\ &\times I_k(|\mathbf{k} - \mathbf{q}_1|, q_1, \tau) I_k(|\mathbf{k} - \mathbf{q}_2|, q_2, \tau) \frac{q_1^2}{|\mathbf{q}_1 - \mathbf{q}_2|} \Theta(2k_* - |\mathbf{q}_1 - \mathbf{q}_2|) \Big|_{q_2=k_*, \cos\theta_2=\mu_{2*}}. \end{aligned} \quad (\text{A.10})$$

Including the deformation factor  $2^2$ , the corresponding GW density parameter reads

$$\begin{aligned} \Omega_{\lambda\lambda'}^{1c-C2}(k) &= \lim_{\tau \rightarrow \infty} \frac{2^2}{48} (k\tau)^2 \overline{\mathcal{P}_{\lambda\lambda'}^{1c-C2}(\tau, k)} \\ &= \frac{3G_{\text{NL}}^2 A_g^4 k^2}{64\pi^2 k_*^4} \int dq_1 d\cos\theta_1 d\varphi Q_{\lambda\lambda'}^2(\mathbf{k}, \mathbf{q}_1, \mathbf{q}_2) \\ &\times \overline{J_k^2(|\mathbf{k} - \mathbf{q}_1|, q_1; |\mathbf{k} - \mathbf{q}_2|, q_2)} \frac{q_1^2}{|\mathbf{q}_1 - \mathbf{q}_2|} \Theta(2k_* - |\mathbf{q}_1 - \mathbf{q}_2|) \Big|_{q_2=k_*, \cos\theta_2=\mu_{2*}}. \end{aligned} \quad (\text{A.11})$$

Its numerical result is shown in Fig. 17.

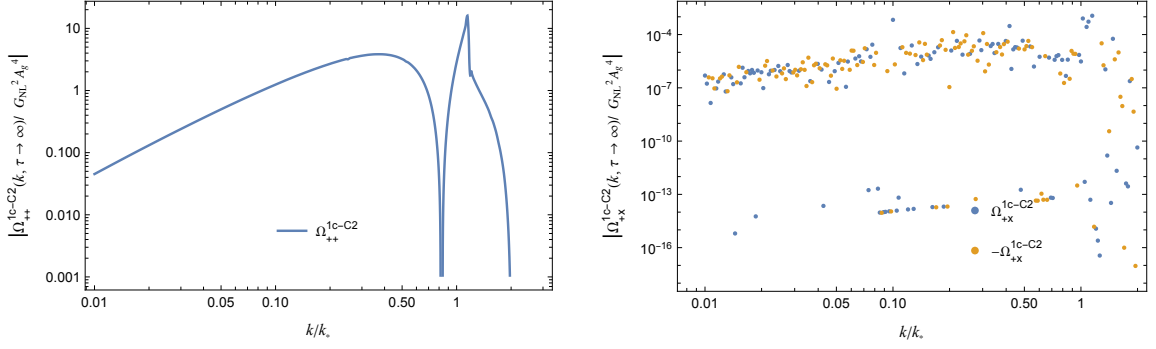


**Figure 17:** The normalized GW amplitudes  $|\Omega_{++}^{1c-C2}/G_{\text{NL}}^2 A_g^4|$  (left) and  $|\Omega_{+x}^{1c-C2}/G_{\text{NL}}^2 A_g^4|$  (right) in the similar style to Fig. 16.

## A.2 1-convolution Z term

The 1c-Z1 and 1c-Z2 terms are given by

$$\begin{aligned}
P_{\lambda\lambda'}^{1c-Z1}(\tau, k) &= \frac{(2!F_{\text{NL}})^2 3!G_{\text{NL}}}{2!} \int \frac{d^3q_1}{(2\pi)^3} \frac{d^3q_2}{(2\pi)^3} \frac{d^3q_3}{(2\pi)^3} Q_\lambda(\mathbf{k}, \mathbf{q}_1) Q_{\lambda'}(\mathbf{k}, \mathbf{q}_2 - \mathbf{q}_1) \\
&\quad \times I_k(|\mathbf{k} - \mathbf{q}_1|, q_1, \tau) I_k(|\mathbf{k} - \mathbf{q}_2 + \mathbf{q}_1|, |\mathbf{q}_2 - \mathbf{q}_1|, \tau) \\
&\quad \quad \quad \times P_g(q_1) P_g(|\mathbf{q}_2 - \mathbf{k}|) P_g(q_3) P_g(|\mathbf{q}_2 - \mathbf{q}_1 - \mathbf{q}_3|), \quad (\text{A.12}) \\
P_{\lambda\lambda'}^{1c-Z2}(\tau, k) &= \frac{(3!G_{\text{NL}})^2}{2!} \int \frac{d^3q_1}{(2\pi)^3} \frac{d^3q_2}{(2\pi)^3} \frac{d^3q_3}{(2\pi)^3} Q_\lambda(\mathbf{k}, \mathbf{q}_1) Q_{\lambda'}(\mathbf{k}, \mathbf{q}_2) \\
&\quad \times I_k(|\mathbf{k} - \mathbf{q}_1|, q_1, \tau) I_k(|\mathbf{k} - \mathbf{q}_2|, q_2, \tau) P_g(q_1) P_g(q_2) P_g(q_3) P_g(|\mathbf{q}_1 + \mathbf{q}_2 - \mathbf{k} - \mathbf{q}_3|).
\end{aligned}$$

$\mathbf{q}_3$  integrations can be again done by Eq. (A.3). For the 1c-Z1 term, the remaining constraints read

$$\delta(\ln q_1 - \ln k_*) \delta(\ln |\mathbf{q}_2 - \mathbf{k}| - \ln k_*) = \frac{k_*^2}{k q_2} \delta(\ln q_1 - \ln k_*) \delta(\cos \theta_2 - \tilde{\mu}_{2*}), \quad (\text{A.13})$$

where  $\tilde{\mu}_{2*} = \frac{q_2^2 + k^2 - k_*^2}{2k q_2}$ . Accordingly, the power spectrum for the 1c-Z1 term can be reduced to

$$\begin{aligned}
\mathcal{P}_{\lambda\lambda'}^{1c-Z1}(\tau, k) &= \frac{3F_{\text{NL}}^2 G_{\text{NL}} A_g^4 k^2}{8\pi^2 k_*^3} \int d \cos \theta_1 d\phi_1 dq_2 d\phi_2 Q_\lambda(\mathbf{k}, \mathbf{q}_1) Q_{\lambda'}(\mathbf{k}, \mathbf{q}_2 - \mathbf{q}_1) \\
&\quad \times I_k(|\mathbf{k} - \mathbf{q}_1|, q_1, \tau) I_k(|\mathbf{k} - \mathbf{q}_2 + \mathbf{q}_1|, |\mathbf{q}_2 - \mathbf{q}_1|, \tau) \frac{q_2 \Theta(2k_* - |\mathbf{q}_2 - \mathbf{q}_1|)}{|\mathbf{q}_2 - \mathbf{q}_1|} \Big|_{q_1=k_*, \cos \theta_2=\tilde{\mu}_{2*}}. \quad (\text{A.14})
\end{aligned}$$

Changing the integration variables from  $\phi_1$  and  $\phi_2$  to  $\varphi = \phi_1 - \phi_2$  and  $\phi_2$ , one finds that the second line does not depend on  $\phi_2$ . Therefore, the polarization factors can be summarized again as a  $\phi_2$  integration of  $Q_\lambda(\mathbf{k}, \mathbf{q}_1) Q_{\lambda'}(\mathbf{k}, \mathbf{q}_2 - \mathbf{q}_1)$ :

$$\tilde{Q}_{\lambda\lambda'}^2(\mathbf{k}, \mathbf{q}_1, \mathbf{q}_2 - \mathbf{q}_1) := \int d\phi_2 Q_\lambda(\mathbf{k}, \mathbf{q}_1) Q_{\lambda'}(\mathbf{k}, \mathbf{q}_2 - \mathbf{q}_1), \quad (\text{A.15})$$

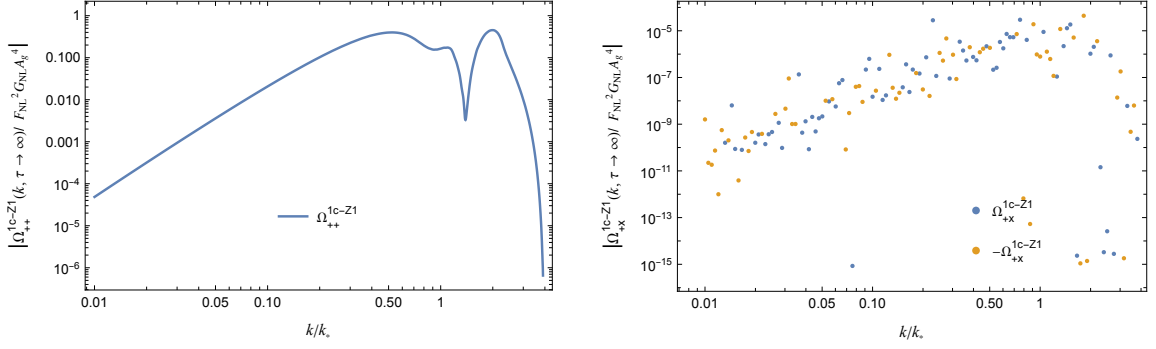


**Figure 18:** The normalized GW amplitudes  $|\Omega_{++}^{1c-Z1}/F_{\text{NL}}^2 G_{\text{NL}} A_g^4|$  (left) and  $|\Omega_{+x}^{1c-Z1}/F_{\text{NL}}^2 G_{\text{NL}} A_g^4|$  (right) in the similar style to Fig. 16

which is obtained as

$$\begin{aligned} \tilde{Q}_{++}^2 &= \tilde{Q}_{\times\times}^2 = \frac{\pi q_1^2 \sin^2 \theta_1}{2} (2q_1 q_2 \sin \theta_1 \sin \theta_2 \cos \varphi + q_1^2 \sin^2 \theta_1 + q_2^2 \sin^2 \theta_2 \cos 2\varphi), \\ \tilde{Q}_{+x}^2 &= -\tilde{Q}_{\times+}^2 = -\pi q_1^2 q_2 \sin \theta_1^2 \sin \theta_2 (-q_1 \sin \theta_1 + q_2 \sin \theta_2 \cos \varphi) \sin \varphi. \end{aligned} \quad (\text{A.16})$$

Including the deformation factor  $2^3$  for the 1c-Z1 term, the density parameter of the induced GW in the RD era can be obtained as follows.

$$\begin{aligned} \Omega_{\lambda\lambda'}^{1c-Z1}(k) &= \lim_{\tau \rightarrow \infty} \frac{2^3}{48} (k\tau)^2 \overline{\mathcal{P}_{\lambda\lambda'}^{1c-Z1}(\tau, k)} \\ &= \frac{F_{\text{NL}}^2 G_{\text{NL}} A_g^4 k^2}{16\pi^2 k_*^3} \int d \cos \theta_1 d\varphi dq_2 \tilde{Q}_{\lambda\lambda'}^2(\mathbf{k}, \mathbf{q}_1, \mathbf{q}_2 - \mathbf{q}_1) \\ &\quad \times \frac{J_k^2(|\mathbf{k} - \mathbf{q}_1|, q_1; |\mathbf{k} - \mathbf{q}_2 + \mathbf{q}_1|, |\mathbf{q}_2 - \mathbf{q}_1|)}{|\mathbf{q}_2 - \mathbf{q}_1|} \Big|_{q_1=k_*, \cos \theta_2=\bar{\mu}_{2*}}. \end{aligned} \quad (\text{A.17})$$

The numerical resultant power spectrum is exhibited in Fig. 18.

For 1c-Z2 term, the remaining constraints after the  $\mathbf{q}_3$  integral are trivial as

$$\delta(\ln q_1 - \ln k_*) \delta(\ln q_2 - \ln k_*). \quad (\text{A.18})$$

The corresponding power spectrum then reads

$$\begin{aligned} \mathcal{P}_{\lambda\lambda'}^{1c-Z2}(\tau, k) &= \frac{9G_{\text{NL}}^2 A_g^4 k^3}{16\pi^2 k_*^2} \int d \cos \theta_1 d\varphi d \cos \theta_2 Q_{\lambda\lambda'}^2(\mathbf{k}, \mathbf{q}_1, \mathbf{q}_2) \\ &\quad \times I_k(|\mathbf{k} - \mathbf{q}_1|, q_1, \tau) I_k(|\mathbf{k} - \mathbf{q}_2|, q_2, \tau) \frac{\Theta(2k_* - |\mathbf{q}_1 + \mathbf{q}_2 - \mathbf{k}|)}{|\mathbf{q}_1 + \mathbf{q}_2 - \mathbf{k}|} \Big|_{q_1=q_2=k_*}. \end{aligned} \quad (\text{A.19})$$

where  $Q_{\lambda\lambda'}^2$  is given by Eq. (A.7).

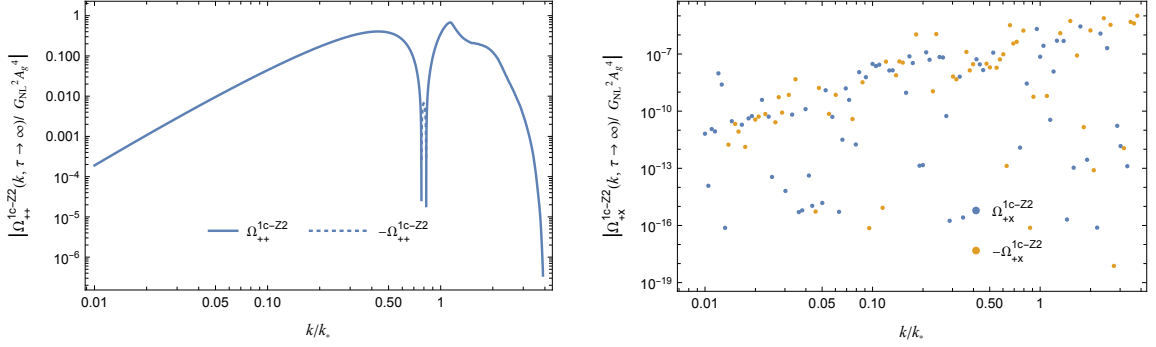


**Figure 19:** The normalized GW amplitudes  $|\Omega_{++}^{1c-Z2}/G_{\text{NL}}^2 A_g^4|$  (left) and  $|\Omega_{+x}^{1c-Z2}/G_{\text{NL}}^2 A_g^4|$  (right) in the similar style to Fig. 16

Including the deformation factor  $2^2$  for the 1c-Z2 term, the density parameter of the induced GWs can be obtained as follows.

$$\begin{aligned}
\Omega_{\lambda\lambda'}^{1c-Z2}(k) &= \lim_{\tau \rightarrow \infty} \frac{2^2}{48} (k\tau)^2 \overline{\mathcal{P}_{\lambda\lambda'}^{1c-Z2}(\tau, k)} \\
&= \frac{3G_{\text{NL}}^2 A_g^4 k^3}{64\pi^2 k_*^2} \int d\cos\theta_1 d\varphi d\cos\theta_2 Q_{\lambda\lambda'}^2(\mathbf{k}, \mathbf{q}_1, \mathbf{q}_2) \\
&\quad \times \frac{J_k^2(|\mathbf{k} - \mathbf{q}_1|, q_1; |\mathbf{k} - \mathbf{q}_2|, q_2)}{|\mathbf{q}_1 - \mathbf{k} + \mathbf{q}_2|} \Bigg|_{q_1=q_2=k_*}. \quad (\text{A.20})
\end{aligned}$$

The numerical resultant power spectrum is shown in Fig. 19.

### A.3 CZ term

The CZ term reads

$$\begin{aligned}
P_{\lambda\lambda'}^{\text{CZ}}(k) &= (2!F_{\text{NL}})^2 3!G_{\text{NL}} \int \frac{d^3q_1}{(2\pi)^3} \frac{d^3q_2}{(2\pi)^3} \frac{d^3q_3}{(2\pi)^3} Q_\lambda(\mathbf{k}, \mathbf{q}_1 + \mathbf{q}_2 + \mathbf{q}_3) Q_{\lambda'}(\mathbf{k}, \mathbf{q}_2) \\
&\quad \times I_k(|\mathbf{k} - \mathbf{q}_1 - \mathbf{q}_2 - \mathbf{q}_3|, |\mathbf{q}_1 + \mathbf{q}_2 + \mathbf{q}_3|, \tau) I_k(|\mathbf{k} - \mathbf{q}_2|, q_2, \tau) \\
&\quad \times P_g(q_1) P_g(q_2) P_g(q_3) P_g(|\mathbf{k} - \mathbf{q}_1 - \mathbf{q}_2|). \quad (\text{A.21})
\end{aligned}$$

Contrary to the 1c-C and 1c-Z terms, it does not have a convolved propagator and hence cannot be simplified easily. We will change integral variables several times to make the most of the momentum constraints.

First of all, the ordinary spherical coordinate takes the  $z$  direction along the  $\mathbf{k}$  direction, but in our case, the last momentum constraint  $|\mathbf{k} - \mathbf{q}_1 - \mathbf{q}_2| = k_*$  can be more easily treated by defining the  $z$  direction along the  $\mathbf{q} := \mathbf{q}_1 + \mathbf{q}_2$  direction. The integral variables are changed to  $(q, \theta_k, \phi_k, q_2, \theta_2, \phi_2, q_3, \theta_3, \phi_3)$  where the relevant vectors are defined by

$$\begin{aligned}
\mathbf{k} &= k \begin{pmatrix} \sin\theta_k \cos\phi_k \\ \sin\theta_k \sin\phi_k \\ \cos\theta_k \end{pmatrix}, \quad \mathbf{q}_2 = q_2 \begin{pmatrix} \sin\theta_2 \cos\phi_2 \\ \sin\theta_2 \sin\phi_2 \\ \cos\theta_2 \end{pmatrix}, \quad \mathbf{q}_3 = q_3 \begin{pmatrix} \sin\theta_3 \cos\phi_3 \\ \sin\theta_3 \sin\phi_3 \\ \cos\theta_3 \end{pmatrix}, \\
\mathbf{q} &= \begin{pmatrix} 0 \\ 0 \\ q \end{pmatrix}, \quad \mathbf{q}_1 = \mathbf{q} - \mathbf{q}_2 = \begin{pmatrix} -q_2 \sin\theta_2 \cos\phi_2 \\ -q_2 \sin\theta_2 \sin\phi_2 \\ q - q_2 \cos\theta_2 \end{pmatrix}. \quad (\text{A.22})
\end{aligned}$$

The Dirac deltas from the power spectra can be recast as

$$\begin{aligned} & \delta(\ln q_1 - \ln k_*) \delta(\ln q_2 - \ln k_*) \delta(\ln q_3 - \ln k_*) \delta(\ln |\mathbf{k} - \mathbf{q}| - \ln k_*) \\ &= \frac{k_*^3}{kq^2} \delta(\cos \theta_2 - \bar{\mu}_{2*}) \delta(\ln q_2 - \ln k_*) \delta(\ln q_3 - \ln k_*) \delta(\cos \theta_k - \mu_{k*}), \end{aligned} \quad (\text{A.23})$$

where

$$\bar{\mu}_{2*} = \frac{q}{2k_*}, \quad \mu_{k*} = \frac{q^2 + k^2 - k_*^2}{2qk}. \quad (\text{A.24})$$

To calculate the polarization part, we consider the rotation back of vectors to the original coordinate where  $\mathbf{k}$  is in the  $z$  direction. The current coordinate is rotated back to the original one by the rotation by  $-\phi_k$  around the  $z$  axis followed by the rotation by  $-\theta_k$  around the  $y$  axis followed by the rotation back by  $\phi_k$  around the  $z$  axis.<sup>5</sup> Any vector  $\mathbf{p}^{(q)}$  is transformed to  $\mathbf{p}^{(k)}$  by these rotations as

$$\begin{aligned} \mathbf{p}^{(q)} \rightarrow \mathbf{p}^{(k)} &= R_{\phi_k} R_{\theta_k}^T R_{\phi_k}^T \mathbf{p}^{(q)} \\ &= \begin{pmatrix} \cos \phi_k & -\sin \phi_k & 0 \\ \sin \phi_k & \cos \phi_k & 0 \\ 0 & 0 & 1 \end{pmatrix} \begin{pmatrix} \cos \theta_k & 0 & -\sin \theta_k \\ 0 & 1 & 0 \\ \sin \theta_k & 0 & \cos \theta_k \end{pmatrix} \begin{pmatrix} \cos \phi_k & \sin \phi_k & 0 \\ -\sin \phi_k & \cos \phi_k & 0 \\ 0 & 0 & 1 \end{pmatrix} \mathbf{p}^{(q)}. \end{aligned} \quad (\text{A.25})$$

The polarization tensors are given in the original coordinate by

$$\epsilon_{ij}^{(k)\lambda}(\mathbf{k}) = \begin{cases} \frac{1}{\sqrt{2}} \begin{pmatrix} 1 & 0 & 0 \\ 0 & -1 & 0 \\ 0 & 0 & 0 \end{pmatrix} & \text{for } \lambda = +, \\ \frac{1}{\sqrt{2}} \begin{pmatrix} 0 & 1 & 0 \\ 1 & 0 & 0 \\ 0 & 0 & 0 \end{pmatrix} & \text{for } \lambda = \times, \end{cases} \quad (\text{A.26})$$

and hence the projection factor  $Q_\lambda(\mathbf{k}, \mathbf{p})$  is written in terms of the  $q$  coordinate expression  $\mathbf{p}^{(q)}$  as

$$Q_\lambda(\mathbf{k}, \mathbf{p}) = \mathbf{p}^{(q)T} R_{\phi_k} R_{\theta_k} R_{\phi_k}^T \epsilon^{(k)\lambda} R_{\phi_k} R_{\theta_k}^T R_{\phi_k}^T \mathbf{p}^{(q)}. \quad (\text{A.27})$$

Now all the relevant quantities are expressed in the new integral variables. With use of the Dirac deltas (A.23), the power spectrum reduces to

$$\begin{aligned} \mathcal{P}_{\lambda\lambda'}^{\text{CZ}}(\tau, k) &= \frac{3F_{\text{NL}}^2 G_{\text{NL}} A_g^4 k^2}{8\pi^3 k_*^2} \int_{|1-\tilde{k}|}^{\min(2, 1+\tilde{k})} d\tilde{q} \int d\phi_k d\phi_2 d\cos\theta_3 d\phi_3 Q_\lambda(\mathbf{k}, \mathbf{q} + \mathbf{q}_3) \\ &\quad \times Q_{\lambda'}(\mathbf{k}, \mathbf{q}_2) I_k(|\mathbf{k} - \mathbf{q} - \mathbf{q}_3|, |\mathbf{q} + \mathbf{q}_3|, \tau) I_k(|\mathbf{k} - \mathbf{q}_2|, q_2, \tau) \Big|_{q_2=q_3=k_*, \cos\theta_2=\bar{\mu}_{2*}, \cos\theta_k=\mu_{k*}}. \end{aligned} \quad (\text{A.28})$$

Note that  $\tilde{q} = q/k_*$ ,  $\tilde{k} = k/k_*$  and the integration region for  $\tilde{q}$  come from the triangle condition on  $\mathbf{q} = \mathbf{q}_1 + \mathbf{q}_2$  with  $q_1 = q_2 = |\mathbf{k} - \mathbf{q}| = k_*$ . Regarding the kernel part, it should be noticed that the norms  $|\mathbf{k} - \mathbf{q} - \mathbf{q}_3|$  and  $|\mathbf{k} - \mathbf{q}_2|$  depend on  $\phi_k$  only through  $\tilde{\phi}_3 := \phi_3 - \phi_k$  and  $\tilde{\phi}_2 := \phi_2 - \phi_k$  respectively as can be seen in the explicit expression

$$\begin{aligned} (\mathbf{k} - \mathbf{q} - \mathbf{q}_3)^2 &= k^2 + q^2 + q_3^2 + 2q_3(q - k \cos \theta_k) \cos \theta_3 - 2k(q \cos \theta_k + q_3 \sin \theta_k \sin \theta_3 \cos \tilde{\phi}_3), \\ (\mathbf{k} - \mathbf{q}_2)^2 &= k^2 + q_2^2 - 2kq_2(\cos \theta_k \cos \theta_2 + \sin \theta_k \sin \theta_2 \cos \tilde{\phi}_2). \end{aligned} \quad (\text{A.29})$$

<sup>5</sup>The last rotation by  $\phi_k$  around the  $z$  axis is necessary for the Jacobian to be  $q^2 q_2^2 q_3^2$ .

Therefore, by changing the integration variables as  $\phi_2 \rightarrow \tilde{\phi}_2$  and  $\phi_3 \rightarrow \tilde{\phi}_3$ , the  $\phi_k$  integration appears only in the projection part:

$$\bar{Q}_{\lambda\lambda'}^2(\mathbf{k}, \mathbf{q} + \mathbf{q}_3, \mathbf{q}_2) := \int d\phi_k Q_\lambda(\mathbf{k}, \mathbf{q} + \mathbf{q}_3) Q_{\lambda'}(\mathbf{k}, \mathbf{q}_2), \quad (\text{A.30})$$

which can be solved as

$$\begin{aligned} \bar{Q}_{++}^2 &= \bar{Q}_{\times\times}^2 \\ &= \frac{\pi q_2^2}{16} \left[ \left( 2 \sin^2 \theta_2 \cos^2 \theta_k \cos^2 \tilde{\phi}_2 - \sin 2\theta_2 \sin 2\theta_k \cos \tilde{\phi}_2 + 2 \cos^2 \theta_2 \sin^2 \theta_k - 2 \sin^2 \theta_2 \sin^2 \tilde{\phi}_2 \right) \right. \\ &\quad \times \left( 4q^2 \sin^2 \theta_k + q_3 \left( -4(q + q_3 \cos \theta_3) \sin \theta_3 \sin 2\theta_k \cos \tilde{\phi}_3 \right. \right. \\ &\quad \left. \left. + (8q \cos \theta_3 + 3q_3 \cos 2\theta_3 + q_3) \sin^2 \theta_k + q_3 (\cos 2\theta_k + 3) \sin^2 \theta_3 \cos 2\tilde{\phi}_3 \right) \right) \\ &\quad \left. + 8q_3 \sin \theta_3 \left( \sin 2\theta_2 \sin \theta_k \sin \tilde{\phi}_2 - \sin^2 \theta_2 \cos \theta_k \sin 2\tilde{\phi}_2 \right) \right. \\ &\quad \left. \times \left( 2(q + q_3 \cos \theta_3) \sin \theta_k \sin \tilde{\phi}_3 - q_3 \sin \theta_3 \cos \theta_k \sin 2\tilde{\phi}_3 \right) \right], \end{aligned} \quad (\text{A.31})$$

and

$$\begin{aligned} \bar{Q}_{+\times}^2 &= -\bar{Q}_{\times+}^2 \\ &= \frac{\pi q_2^2}{32} \left[ \left( 4 \sin^2 \theta_2 \cos \theta_k \sin 2\tilde{\phi}_2 - 4 \sin 2\theta_2 \sin \theta_k \sin \tilde{\phi}_2 \right) \right. \\ &\quad \times \left( 4q^2 \sin^2 \theta_k + q_3 \left( -4(q + q_3 \cos \theta_3) \sin \theta_3 \sin 2\theta_k \cos \tilde{\phi}_3 \right. \right. \\ &\quad \left. \left. + (8q \cos \theta_3 + 3q_3 \cos 2\theta_3 + q_3) \sin^2 \theta_k + q_3 (\cos 2\theta_k + 3) \sin^2 \theta_3 \cos 2\tilde{\phi}_3 \right) \right) \\ &\quad \left. + 4q_3 \sin \theta_3 \left( (\cos 2\theta_k + 3) \sin^2 \theta_2 \cos 2\tilde{\phi}_2 - 2 \sin 2\theta_2 \sin 2\theta_k \cos \tilde{\phi}_2 + (3 \cos 2\theta_2 + 1) \sin^2 \theta_k \right) \right. \\ &\quad \left. \times \left( 2(q + q_3 \cos \theta_3) \sin \theta_k \sin \tilde{\phi}_3 - q_3 \sin \theta_3 \cos \theta_k \sin 2\tilde{\phi}_3 \right) \right]. \end{aligned} \quad (\text{A.32})$$

Including the deformation factor  $2^3$ , the GW density parameter is given by

$$\begin{aligned} \Omega_{\lambda\lambda'}^{\text{CZ}}(k) &= \lim_{\tau \rightarrow \infty} \frac{2^3}{48} (k\tau)^2 \overline{\mathcal{P}_{\lambda\lambda'}^{\text{CZ}}(\tau, k)} \\ &= \frac{F_{\text{NL}}^2 G_{\text{NL}} A_g^4 k^2}{16\pi^3 k_*^2} \int_{|1-\tilde{k}|}^{\min(2, 1+\tilde{k})} d\tilde{q} \int d\phi_2 d\cos\theta_3 d\phi_3 \bar{Q}_{\lambda\lambda'}^2(\mathbf{k}, \mathbf{q} + \mathbf{q}_3, \mathbf{q}_2) \\ &\quad \times \overline{J_k^2(|\mathbf{k} - \mathbf{q} - \mathbf{q}_3|, |\mathbf{q} + \mathbf{q}_3|; |\mathbf{k} - \mathbf{q}_2|, q_2)} \Big|_{q_2=q_3=k_*, \cos\theta_2=\bar{\mu}_{2*}, \cos\theta_k=\mu_{k*}}. \end{aligned} \quad (\text{A.33})$$

Its numerical result is shown in Fig. 20.

## References

- [1] N. Kitajima, Y. Tada, S. Yokoyama and C.-M. Yoo, *Primordial black holes in peak theory with a non-Gaussian tail*, *JCAP* **10** (2021) 053 [2109.00791].

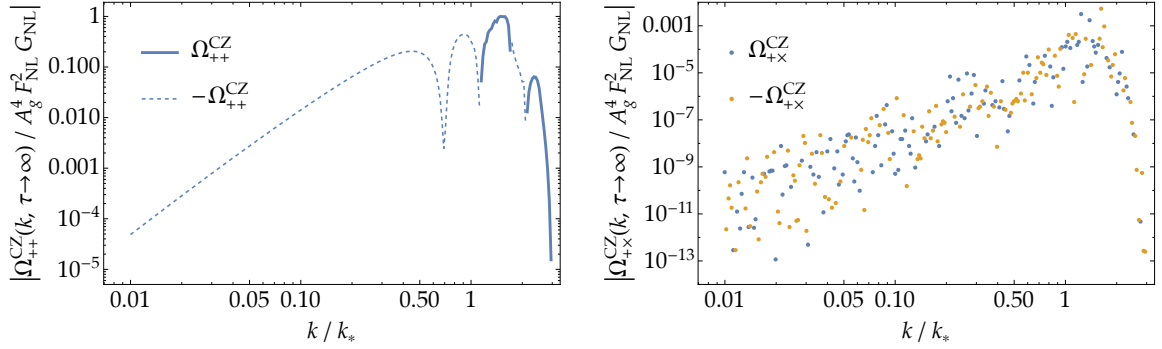


**Figure 20:** The normalized GW amplitudes  $|\Omega_{++}^{\text{CZ}}/F_{\text{NL}}^2 G_{\text{NL}} A_g^4|$  (left) and  $|\Omega_{+\times}^{\text{CZ}}/F_{\text{NL}}^2 G_{\text{NL}} A_g^4|$  (right) in the similar style to Fig. 16. The wavy feature around the maximum of the left panel is due to numerical errors.

- [2] B.J. Carr and S.W. Hawking, *Black holes in the early Universe*, *Mon. Not. Roy. Astron. Soc.* **168** (1974) 399.
- [3] B.J. Carr, *The Primordial black hole mass spectrum*, *Astrophys. J.* **201** (1975) 1.
- [4] B. Carr, K. Kohri, Y. Sendouda and J. Yokoyama, *Constraints on primordial black holes*, *Rept. Prog. Phys.* **84** (2021) 116902 [2002.12778].
- [5] P. Amaro-Seoane et al., *Laser Interferometer Space Antenna*, *arXiv e-prints* (2017) arXiv:1702.00786 [1702.00786].
- [6] TIANQIN collaboration, *TianQin: a space-borne gravitational wave detector*, *Class. Quant. Grav.* **33** (2016) 035010 [1512.02076].
- [7] W.-H. Ruan, Z.-K. Guo, R.-G. Cai and Y.-Z. Zhang, *Taiji program: Gravitational-wave sources*, *Int. J. Mod. Phys. A* **35** (2020) 2050075 [1807.09495].
- [8] S. Kawamura et al., *Current status of space gravitational wave antenna DECIGO and B-DECIGO*, *PTEP* **2021** (2021) 05A105 [2006.13545].
- [9] L. Badurina et al., *AION: An Atom Interferometer Observatory and Network*, *JCAP* **05** (2020) 011 [1911.11755].
- [10] MAGIS-100 collaboration, *Matter-wave Atomic Gradiometer Interferometric Sensor (MAGIS-100)*, *Quantum Sci. Technol.* **6** (2021) 044003 [2104.02835].
- [11] KAGRA, LIGO SCIENTIFIC, VIRGO, VIRGO collaboration, *Prospects for observing and localizing gravitational-wave transients with Advanced LIGO, Advanced Virgo and KAGRA*, *Living Rev. Rel.* **21** (2018) 3 [1304.0670].
- [12] M. Punturo et al., *The Einstein Telescope: A third-generation gravitational wave observatory*, *Class. Quant. Grav.* **27** (2010) 194002.
- [13] D. Reitze et al., *Cosmic Explorer: The U.S. Contribution to Gravitational-Wave Astronomy beyond LIGO*, *Bull. Am. Astron. Soc.* **51** (2019) 035 [1907.04833].
- [14] J.P.W. Verbiest, S. Osłowski and S. Burke-Spolaor, *Pulsar Timing Array Experiments*, in *Handbook of Gravitational Wave Astronomy*, p. 4 (2021), DOI.
- [15] R. Saito and J. Yokoyama, *Gravitational-Wave Constraints on the Abundance of Primordial Black Holes*, *Prog. Theor. Phys.* **123** (2010) 867 [0912.5317].
- [16] N. Bartolo, V. De Luca, G. Franciolini, A. Lewis, M. Peloso and A. Riotto, *Primordial Black Hole Dark Matter: LISA Serendipity*, *Phys. Rev. Lett.* **122** (2019) 211301 [1810.12218].

- [17] T. Nakama, J. Silk and M. Kamionkowski, *Stochastic gravitational waves associated with the formation of primordial black holes*, *Phys. Rev. D* **95** (2017) 043511 [[1612.06264](#)].
- [18] V. Vennin, *Stochastic inflation and primordial black holes*, other thesis, 9, 2020, [[2009.08715](#)].
- [19] Y.-F. Cai, X. Chen, M.H. Namjoo, M. Sasaki, D.-G. Wang and Z. Wang, *Revisiting non-Gaussianity from non-attractor inflation models*, *JCAP* **05** (2018) 012 [[1712.09998](#)].
- [20] V. Atal, J. Garriga and A. Marcos-Caballero, *Primordial black hole formation with non-Gaussian curvature perturbations*, *JCAP* **09** (2019) 073 [[1905.13202](#)].
- [21] V. Atal, J. Cid, A. Escrivà and J. Garriga, *PBH in single field inflation: the effect of shape dispersion and non-Gaussianities*, *JCAP* **05** (2020) 022 [[1908.11357](#)].
- [22] M. Biagetti, V. De Luca, G. Franciolini, A. Kehagias and A. Riotto, *The formation probability of primordial black holes*, *Phys. Lett. B* **820** (2021) 136602 [[2105.07810](#)].
- [23] R.-g. Cai, S. Pi and M. Sasaki, *Gravitational Waves Induced by non-Gaussian Scalar Perturbations*, *Phys. Rev. Lett.* **122** (2019) 201101 [[1810.11000](#)].
- [24] C. Unal, *Imprints of Primordial Non-Gaussianity on Gravitational Wave Spectrum*, *Phys. Rev. D* **99** (2019) 041301 [[1811.09151](#)].
- [25] P. Adshead, K.D. Lozanov and Z.J. Weiner, *Non-Gaussianity and the induced gravitational wave background*, *JCAP* **10** (2021) 080 [[2105.01659](#)].
- [26] C. Yuan and Q.-G. Huang, *Gravitational waves induced by the local-type non-Gaussian curvature perturbations*, *Phys. Lett. B* **821** (2021) 136606 [[2007.10686](#)].
- [27] V. Atal and G. Domènech, *Probing non-Gaussianities with the high frequency tail of induced gravitational waves*, *JCAP* **06** (2021) 001 [[2103.01056](#)].
- [28] S. Garcia-Saenz, L. Pinol, S. Renaux-Petel and D. Werth, *No-go Theorem for Scalar-Trispectrum-Induced Gravitational Waves*, [2207.14267](#).
- [29] G. Domènech, *Scalar Induced Gravitational Waves Review*, *Universe* **7** (2021) 398 [[2109.01398](#)].
- [30] PLANCK collaboration, *Planck 2018 results. IX. Constraints on primordial non-Gaussianity*, *Astron. Astrophys.* **641** (2020) A9 [[1905.05697](#)].
- [31] A.A. Starobinsky, *Dynamics of Phase Transition in the New Inflationary Universe Scenario and Generation of Perturbations*, *Phys. Lett. B* **117** (1982) 175.
- [32] A.A. Starobinsky, *Multicomponent de Sitter (Inflationary) Stages and the Generation of Perturbations*, *JETP Lett.* **42** (1985) 152.
- [33] M. Sasaki and E.D. Stewart, *A General analytic formula for the spectral index of the density perturbations produced during inflation*, *Prog. Theor. Phys.* **95** (1996) 71 [[astro-ph/9507001](#)].
- [34] D. Wands, K.A. Malik, D.H. Lyth and A.R. Liddle, *A New approach to the evolution of cosmological perturbations on large scales*, *Phys. Rev. D* **62** (2000) 043527 [[astro-ph/0003278](#)].
- [35] D.H. Lyth, K.A. Malik and M. Sasaki, *A General proof of the conservation of the curvature perturbation*, *JCAP* **05** (2005) 004 [[astro-ph/0411220](#)].
- [36] A.D. Linde, *NONSINGULAR REGENERATING INFLATIONARY UNIVERSE* (7, 1982).
- [37] P.J. Steinhardt, *NATURAL INFLATION*, in *Nuffield Workshop on the Very Early Universe*, 7, 1982.
- [38] A. Vilenkin, *The Birth of Inflationary Universes*, *Phys. Rev. D* **27** (1983) 2848.
- [39] A.D. Linde, *ETERNAL CHAOTIC INFLATION*, *Mod. Phys. Lett. A* **1** (1986) 81.
- [40] A.D. Linde, *ETERNALLY EXISTING SELFREPRODUCING INFLATIONARY UNIVERSE*, *Phys. Scripta T* **15** (1987) 169.



- [41] A.S. Goncharov, A.D. Linde and V.F. Mukhanov, *The Global Structure of the Inflationary Universe*, *Int. J. Mod. Phys. A* **2** (1987) 561.
- [42] G. Barenboim, W.-I. Park and W.H. Kinney, *Eternal Hilltop Inflation*, *JCAP* **05** (2016) 030 [[1601.08140](#)].
- [43] A.A. Starobinsky, *STOCHASTIC DE SITTER (INFLATIONARY) STAGE IN THE EARLY UNIVERSE*, *Lect. Notes Phys.* **246** (1986) 107.
- [44] Y. Nambu and M. Sasaki, *Stochastic Stage of an Inflationary Universe Model*, *Phys. Lett. B* **205** (1988) 441.
- [45] Y. Nambu and M. Sasaki, *Stochastic Approach to Chaotic Inflation and the Distribution of Universes*, *Phys. Lett. B* **219** (1989) 240.
- [46] H.E. Kandrup, *STOCHASTIC INFLATION AS A TIME DEPENDENT RANDOM WALK*, *Phys. Rev. D* **39** (1989) 2245.
- [47] K.-i. Nakao, Y. Nambu and M. Sasaki, *Stochastic Dynamics of New Inflation*, *Prog. Theor. Phys.* **80** (1988) 1041.
- [48] Y. Nambu, *Stochastic Dynamics of an Inflationary Model and Initial Distribution of Universes*, *Prog. Theor. Phys.* **81** (1989) 1037.
- [49] S. Mollerach, S. Matarrese, A. Ortolan and F. Lucchin, *Stochastic inflation in a simple two field model*, *Phys. Rev. D* **44** (1991) 1670.
- [50] A.D. Linde, D.A. Linde and A. Mezhlumian, *From the Big Bang theory to the theory of a stationary universe*, *Phys. Rev. D* **49** (1994) 1783 [[gr-qc/9306035](#)].
- [51] A.A. Starobinsky and J. Yokoyama, *Equilibrium state of a selfinteracting scalar field in the De Sitter background*, *Phys. Rev. D* **50** (1994) 6357 [[astro-ph/9407016](#)].
- [52] C. Pattison, V. Vennin, H. Assadullahi and D. Wands, *Quantum diffusion during inflation and primordial black holes*, *JCAP* **10** (2017) 046 [[1707.00537](#)].
- [53] J.M. Ezquiaga, J. García-Bellido and V. Vennin, *The exponential tail of inflationary fluctuations: consequences for primordial black holes*, *JCAP* **03** (2020) 029 [[1912.05399](#)].
- [54] C. Pattison, V. Vennin, D. Wands and H. Assadullahi, *Ultra-slow-roll inflation with quantum diffusion*, *JCAP* **04** (2021) 080 [[2101.05741](#)].
- [55] D.G. Figueroa, S. Raatikainen, S. Rasanen and E. Tomberg, *Non-Gaussian Tail of the Curvature Perturbation in Stochastic Ultraslow-Roll Inflation: Implications for Primordial Black Hole Production*, *Phys. Rev. Lett.* **127** (2021) 101302 [[2012.06551](#)].
- [56] D.G. Figueroa, S. Raatikainen, S. Rasanen and E. Tomberg, *Implications of stochastic effects for primordial black hole production in ultra-slow-roll inflation*, *JCAP* **05** (2022) 027 [[2111.07437](#)].
- [57] Y. Tada and V. Vennin, *Statistics of coarse-grained cosmological fields in stochastic inflation*, *JCAP* **02** (2022) 021 [[2111.15280](#)].
- [58] J.H.P. Jackson, H. Assadullahi, K. Koyama, V. Vennin and D. Wands, *Numerical simulations of stochastic inflation using importance sampling*, [2206.11234](#).
- [59] N. Ahmadi, M. Noorbala, N. Feyzabadi, F. Eghbalpoor and Z. Ahmadi, *Quantum diffusion in sharp transition to non-slow-roll phase*, *JCAP* **08** (2022) 078 [[2207.10578](#)].
- [60] S. Hooshangi, M.H. Namjoo and M. Noorbala, *Rare events are nonperturbative: Primordial black holes from heavy-tailed distributions*, *Phys. Lett. B* **834** (2022) 137400 [[2112.04520](#)].
- [61] Y.-F. Cai, X.-H. Ma, M. Sasaki, D.-G. Wang and Z. Zhou, *One Small Step for an Inflaton, One Giant Leap for Inflation: a novel non-Gaussian tail and primordial black holes*, [2112.13836](#).

- [62] Y.-F. Cai, X.-H. Ma, M. Sasaki, D.-G. Wang and Z. Zhou, *Highly non-Gaussian tails and primordial black holes from single-field inflation*, [2207.11910](#).
- [63] J.M. Bardeen, J.R. Bond, N. Kaiser and A.S. Szalay, *The Statistics of Peaks of Gaussian Random Fields*, *Astrophys. J.* **304** (1986) 15.
- [64] C.-M. Yoo, T. Harada, J. Garriga and K. Kohri, *Primordial black hole abundance from random Gaussian curvature perturbations and a local density threshold*, *PTEP* **2018** (2018) 123E01 [[1805.03946](#)].
- [65] C.-M. Yoo, J.-O. Gong and S. Yokoyama, *Abundance of primordial black holes with local non-Gaussianity in peak theory*, *JCAP* **09** (2019) 033 [[1906.06790](#)].
- [66] C.-M. Yoo, T. Harada, S. Hirano and K. Kohri, *Abundance of Primordial Black Holes in Peak Theory for an Arbitrary Power Spectrum*, *PTEP* **2021** (2021) 013E02 [[2008.02425](#)].
- [67] A. Escrivà, Y. Tada, S. Yokoyama and C.-M. Yoo, *Simulation of primordial black holes with large negative non-Gaussianity*, *JCAP* **05** (2022) 012 [[2202.01028](#)].
- [68] A. Escrivà, C. Germani and R.K. Sheth, *Universal threshold for primordial black hole formation*, *Phys. Rev. D* **101** (2020) 044022 [[1907.13311](#)].
- [69] M.W. Choptuik, *Universality and scaling in gravitational collapse of a massless scalar field*, *Phys. Rev. Lett.* **70** (1993) 9.
- [70] C.R. Evans and J.S. Coleman, *Observation of critical phenomena and selfsimilarity in the gravitational collapse of radiation fluid*, *Phys. Rev. Lett.* **72** (1994) 1782 [[gr-qc/9402041](#)].
- [71] T. Koike, T. Hara and S. Adachi, *Critical behavior in gravitational collapse of radiation fluid: A Renormalization group (linear perturbation) analysis*, *Phys. Rev. Lett.* **74** (1995) 5170 [[gr-qc/9503007](#)].
- [72] J.C. Niemeyer and K. Jedamzik, *Near-critical gravitational collapse and the initial mass function of primordial black holes*, *Phys. Rev. Lett.* **80** (1998) 5481 [[astro-ph/9709072](#)].
- [73] J.C. Niemeyer and K. Jedamzik, *Dynamics of primordial black hole formation*, *Phys. Rev. D* **59** (1999) 124013 [[astro-ph/9901292](#)].
- [74] I. Hawke and J.M. Stewart, *The dynamics of primordial black hole formation*, *Class. Quant. Grav.* **19** (2002) 3687.
- [75] I. Musco, J.C. Miller and A.G. Polnarev, *Primordial black hole formation in the radiative era: Investigation of the critical nature of the collapse*, *Class. Quant. Grav.* **26** (2009) 235001 [[0811.1452](#)].
- [76] Y. Tada and S. Yokoyama, *Primordial black hole tower: Dark matter, earth-mass, and LIGO black holes*, *Phys. Rev. D* **100** (2019) 023537 [[1904.10298](#)].
- [77] B. Carr and F. Kuhnel, *Primordial black holes as dark matter candidates*, *SciPost Phys. Lect. Notes* **48** (2022) 1 [[2110.02821](#)].
- [78] S. Matarrese, S. Mollerach and M. Bruni, *Second order perturbations of the Einstein-de Sitter universe*, *Phys. Rev. D* **58** (1998) 043504 [[astro-ph/9707278](#)].
- [79] L. Boubekeur, P. Creminelli, J. Norena and F. Vernizzi, *Action approach to cosmological perturbations: the 2nd order metric in matter dominance*, *JCAP* **08** (2008) 028 [[0806.1016](#)].
- [80] F. Arroja, H. Assadullahi, K. Koyama and D. Wands, *Cosmological matching conditions for gravitational waves at second order*, *Phys. Rev. D* **80** (2009) 123526 [[0907.3618](#)].
- [81] J.-C. Hwang, D. Jeong and H. Noh, *Gauge dependence of gravitational waves generated from scalar perturbations*, *Astrophys. J.* **842** (2017) 46 [[1704.03500](#)].
- [82] G. Domènech and M. Sasaki, *Hamiltonian approach to second order gauge invariant cosmological perturbations*, *Phys. Rev. D* **97** (2018) 023521 [[1709.09804](#)].

- [83] J.-O. Gong, *Analytic Integral Solutions for Induced Gravitational Waves*, *Astrophys. J.* **925** (2022) 102 [[1909.12708](#)].
- [84] K. Tomikawa and T. Kobayashi, *Gauge dependence of gravitational waves generated at second order from scalar perturbations*, *Phys. Rev. D* **101** (2020) 083529 [[1910.01880](#)].
- [85] K. Inomata and T. Terada, *Gauge Independence of Induced Gravitational Waves*, *Phys. Rev. D* **101** (2020) 023523 [[1912.00785](#)].
- [86] C. Yuan, Z.-C. Chen and Q.-G. Huang, *Scalar induced gravitational waves in different gauges*, *Phys. Rev. D* **101** (2020) 063018 [[1912.00885](#)].
- [87] Z. Chang, S. Wang and Q.-H. Zhu, *Gauge Invariant Second Order Gravitational Waves*, [2009.11994](#).
- [88] Z. Chang, S. Wang and Q.-H. Zhu, *On the Gauge Invariance of Scalar Induced Gravitational Waves: Gauge Fixings Considered*, [2010.01487](#).
- [89] G. Domènech and M. Sasaki, *Approximate gauge independence of the induced gravitational wave spectrum*, *Phys. Rev. D* **103** (2021) 063531 [[2012.14016](#)].
- [90] C. Yuan, Z.-C. Chen and Q.-G. Huang, *Probing primordial-black-hole dark matter with scalar induced gravitational waves*, *Phys. Rev. D* **100** (2019) 081301 [[1906.11549](#)].
- [91] J.-Z. Zhou, X. Zhang, Q.-H. Zhu and Z. Chang, *The third order scalar induced gravitational waves*, *JCAP* **05** (2022) 013 [[2106.01641](#)].
- [92] Z. Chang, X. Zhang and J.-Z. Zhou, *Primordial black holes and third order scalar induced gravitational waves*, [2209.12404](#).
- [93] K. Kohri and T. Terada, *Semianalytic calculation of gravitational wave spectrum nonlinearly induced from primordial curvature perturbations*, *Phys. Rev. D* **97** (2018) 123532 [[1804.08577](#)].
- [94] J.R. Espinosa, D. Racco and A. Riotto, *A Cosmological Signature of the SM Higgs Instability: Gravitational Waves*, *JCAP* **09** (2018) 012 [[1804.07732](#)].
- [95] G. Domènech, S. Passaglia and S. Renaux-Petel, *Gravitational waves from dark matter isocurvature*, *JCAP* **03** (2022) 023 [[2112.10163](#)].
- [96] K. Schmitz, *New Sensitivity Curves for Gravitational-Wave Signals from Cosmological Phase Transitions*, *JHEP* **01** (2021) 097 [[2002.04615](#)].
- [97] C.T. Byrnes, P.S. Cole and S.P. Patil, *Steepest growth of the power spectrum and primordial black holes*, *JCAP* **06** (2019) 028 [[1811.11158](#)].